JACS Au
AN OPEN ACCESS JOURNAL OF THE AMERICAN CHEMICAL SOCIETY

Open Access
This article is licensed under CC-BY-NC-ND 4.0

pubs.acs.org/jacsau
Article

Of Glasses and Crystals: Mitigating the Deactivation of CaO-Based CO_2 Sorbents through Calcium Aluminosilicates

Maximilian Krödel,[§] César Leroy,[§] Sung Min Kim, Muhammad Awais Naeem, Agnieszka Kierzkowska, Yi-Hsuan Wu, Andac Armutlulu, Alexey Fedorov,* Pierre Florian,* and Christoph R. Müller*

Cite This: *JACS Au* 2023, 3, 3111−3126

Read Online

ACCESS | Metrics & More | Article Recommendations | Supporting Information

ABSTRACT: CaO-based sorbents are cost-efficient materials for high-temperature CO_2 capture, yet they rapidly deactivate over carbonation-regeneration cycles due to sintering, hindering their utilization at the industrial scale. Morphological stabilizers such as Al_2O_3 or SiO_2 (e.g., introduced via impregnation) can improve sintering resistance, but the sorbents still deactivate through the formation of mixed oxide phases and phase segregation, rendering the stabilization inefficient. Here, we introduce a strategy to mitigate these deactivation mechanisms by applying $(Al,Si)O_x$ overcoats via atomic layer deposition onto $CaCO_3$ nanoparticles and benchmark the CO_2 uptake of the resulting sorbent after 10 carbonation-regeneration cycles against sorbents with optimized overcoats of only alumina/silica (+25%) and unstabilized $CaCO_3$ nanoparticles (+55%). ^{27}Al and ^{29}Si NMR studies reveal that the improved CO_2 uptake and structural stability of sorbents with $(Al,Si)O_x$ overcoats is linked to the formation of glassy calcium aluminosilicate phases $(Ca,Al,Si)O_x$ that prevent sintering and phase segregation, probably due to a slower self-diffusion of cations in the glassy phases, reducing in turn the formation of CO_2 capture-inactive Ca-containing mixed oxides. This strategy provides a roadmap for the design of more efficient CaO-based sorbents using glassy stabilizers.

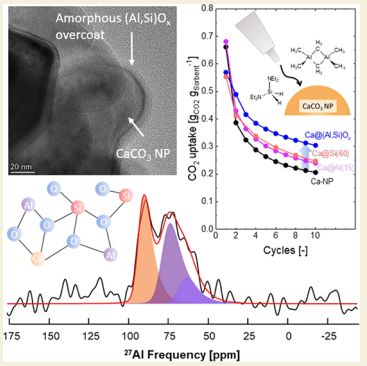

KEYWORDS: *CaO, CO_2 capture, NMR, calcium aluminosilicate, atomic layer deposition (ALD), stabilization*

INTRODUCTION

Anthropogenic emissions of carbon dioxide have increased continuously since the Industrial Revolution and are the principal contributor to climate change.[1,2] To mitigate climate change and the associated rise in global average temperatures and sea levels, CO_2 emissions must be reduced dramatically. In this context, carbon dioxide capture and storage (CCS) technologies are considered a short- to midterm solution to reduce global anthropogenic CO_2 emissions.[1,3,4] The benchmark technology for CO_2 capture at large point sources, such as coal-fired power plants or chemical plants, is amine scrubbing, with capture costs in the range of approximately 40−50 USD per ton of CO_2 captured.[5] However, energy losses arising from the heating of the solvent (water) during regeneration, toxic decomposition products, and a limited long-term stability of amines are among the major disadvantages of this process.[5−7] Thus, alternative processes for CO_2 capture have been explored including the use of cost-effective, environmentally benign, and naturally abundant (in the form of limestone) calcium oxide-based sorbents.[8−10] Owing to the high gravimetric CO_2 uptake of CaO of 0.78 g_{CO2} $g_{sorbent}^{-1}$, the CO_2 capture costs of the so-called calcium looping (CL) process have been estimated to be in the range of 20−30 USD per ton of CO_2 captured, making it an attractive alternative to amine scrubbing.[11]

The CL process utilizes the reversible reaction between CaO and CO_2, *viz.* $CaO_{(s)} + CO_{2(g)} \rightleftarrows CaCO_{3(s)}$ ($\Delta H_R^{298K} = -178$ kJ mol^{-1} for the forward reaction) whereby the CO_2 capture step, i.e. the carbonation of CaO, is typically performed at a temperature in the range of 600−700 °C using a typical flue gas stream of a coal-fired combustion plant (∼10−15 vol % CO_2). To yield a pure stream of CO_2 in the regeneration step, temperatures above 900 °C are required but could be reduced when regenerating in steam or (partial) vacuum.[9,12−15] Due to the high operating temperatures of the process, CaO rapidly deactivates via sintering, leading to a reduction in both surface area and pore volume of the material, which are both linked directly to the carbonation rate (and total gravimetric CO_2 uptake) of the sorbent.[9,16] Therefore, recent material engineering efforts have been focused on alleviating the degree of sintering of CaO-based sorbents to lower CO_2 capture costs.[9,17]

To this end, intermixing CaO with high Tamman-temperature, T_T, stabilizers (i.e., T_T (stabilizer) ≫ T_T ($CaCO_3$) = 533

Received: August 14, 2023
Revised: October 25, 2023
Accepted: October 25, 2023
Published: November 10, 2023

ACS Publications
© 2023 The Authors. Published by American Chemical Society

https://doi.org/10.1021/jacsau.3c00475
JACS Au 2023, 3, 3111−3126

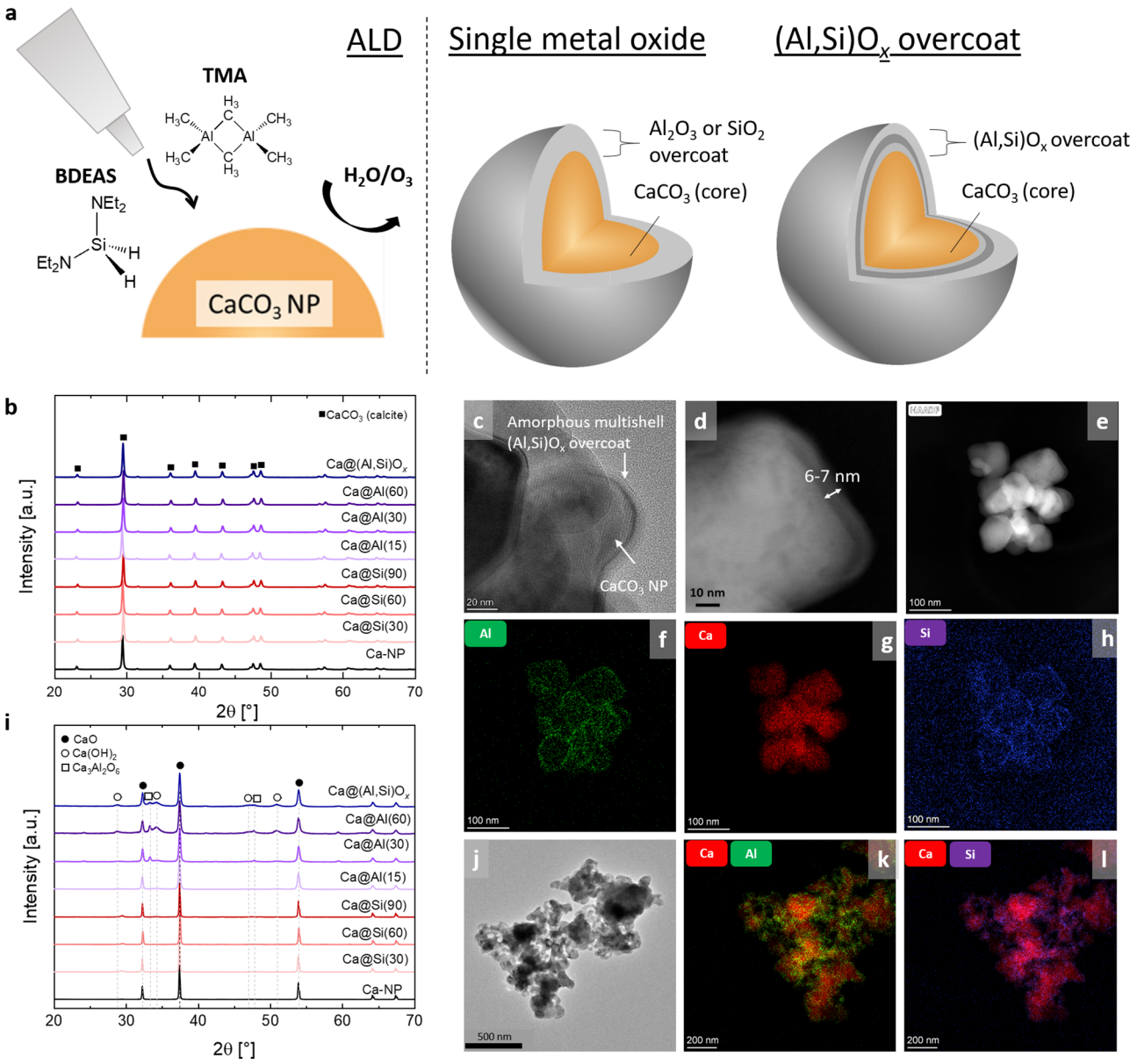

Figure 1. (a) Schematic representation of the use of ALD to engineer overcoats of Al_2O_3, SiO_2 or a mixture of these two oxides, $(Al,Si)O_x$, on $CaCO_3$ NPs. (b) XRD patterns of as-prepared Ca@Si, Ca@Al and Ca@$(Al,Si)O_x$, (c) high-resolution TEM micrograph of as-prepared Ca@$(Al,Si)O_x$ visualizing the deposition of an amorphous overcoat, (d) HAADF micrograph of Ca@$(Al,Si)O_x$ showing the thickness of the mixed $(Al,Si)O_x$ overcoat, (e–h) HAADF micrograph and EDX-TEM elemental mapping of Ca, Al and Si of as-prepared Ca@$(Al,Si)O_x$, (i) XRD patterns of Ca@Si, Ca@Al and Ca@$(Al,Si)O_x$ after the initial heat treatment in N_2 at 900 °C, (j) TEM micrograph of Ca@$(Al,Si)O_x$ after the initial heat treatment and (k–l) EDX-TEM elemental mapping of Al and Si in Ca@$(Al,Si)O_x$ after the initial heat treatment.

°C) such as Al_2O_3, ZrO_2, SiO_2 or MgO (T_T = 899, 1218, 718 and 1118 °C, respectively) has been explored,[18−23] yet, it has not been possible to fully avoid deactivation over cycling through this approach. Further, in such stabilized materials, deactivation can also proceed via the (gradual) formation of mixed oxide(s) between the stabilizer and CaO, leading to the loss of CO_2-capture-active CaO. It has also been reported that the formation of CO_2-capture-inactive mixed oxide can lead to an unfavorable, i.e., heterogeneous, distribution of the stabilizing phase in the sorbent owing to segregation and agglomeration of the (stabilizing) mixed oxide phases upon their formation.[19,21] In such a scenario, deactivation is often exacerbated by the inferior stabilizing properties (e.g., a lower Tammann temperature) of the mixed oxide phase relative to the initially added stabilizer phase.[9] For example, it has been observed that in Al_2O_3-stabilized CaO the mixed oxides $Ca_3Al_2O_6$ and $Ca_{12}Al_{14}O_{33}$ form during cycling, thereby reducing appreciably the quantity of CO_2-capture-active CaO.[21] Further, the $(Ca,Al)O_x$ phases formed show a tendency for surface segregation coupled with particle growth of the mixed oxides (to several hundreds of nanometers in diameter), reducing in turn their effectiveness in preventing the sintering of CaO.[20,21,24] However, also in the case that the stabilizer does not form a mixed phase with CaO (e.g., MgO), surface segregation and agglomeration of the stabilizer with cycling have been reported.[19] As similar deactivation routes have been observed in ZrO_2- and SiO_2-stabilized CaO as well, the described phenomena appear to be a common issue in stabilized CaO-based sorbents, reducing their attractiveness for potential industrial deployment.[9,25−28]

https://doi.org/10.1021/jacsau.3c00475
JACS Au 2023, 3, 3111−3126

As indicated above, the surface area and pore volume of CaO-based sorbents and changes thereof with cycling (and sintering) are arguably the most important descriptors that control their cyclic CO_2 uptake.[8,9] Hence, attempts have been made to introduce porosity into CaO, e.g., by using sacrificial templates.[29−31] To improve the structural stability of the morphology of sorbents and to limit segregation of the stabilizing phases, the combination of the introduction of metal oxide stabilizers and nanostructuring approaches such as core−shell, hollow-shell, and yolk−shell-type architectures have been explored.[20,29,31−36] For example, a MgO-stabilized (11 wt %) multishell-type architecture of CaO yielded a CO_2 uptake of approximately 0.64 g_{CO2} $g_{sorbent}^{-1}$ after 10 carbonation-regeneration cycles, which corresponds to a notable 400% increase in CO_2 uptake compared to the benchmark limestone.[31] Using atomic layer deposition (ALD) to allow for both the nanostructuring of the sorbents and the use of a stabilizer, it has been demonstrated that nanometer-thin metal oxide layers (e.g., Al_2O_3) can appreciably stabilize the cyclic CO_2 uptake of CaO-based sorbents.[20,37] Furthermore, such fabrication of well-defined, model, nanostructured CaO-based sorbents has contributed to the elucidation of deactivation mechanisms in stabilized CaO-based sorbents.[29,31,33] That being said, efficient measures to mitigate the segregation and (surface) agglomeration of the stabilizer and/or mixed phases are currently lacking, not least because we still have an incomplete fundamental understanding of the underlying interactions between CaO and the stabilizer phases and their dynamics under CO_2 capture-regeneration conditions.

In this work, we describe the synthesis and in-depth characterization of well-defined, model metal-oxide-stabilized CaO-based sorbents with the aim to correlate structural features of the stabilizing phase(s) with their effectiveness in maintaining a high CO_2 uptake. To this end, core−shell architectures in which the thickness of the shells containing the stabilizing phase (i.e., Al_2O_3, SiO_2, or mixed $(Al,Si)O_x$) is precisely controlled by ALD are prepared. A practically relevant observation is that sorbents overcoated by mixed $(Al,Si)O_x$ shells feature a significantly reduced decay of the cyclic CO_2 uptake over repeated carbonation-regeneration cycles relative to sorbents that contain a single metal-oxide (Al_2O_3 or SiO_2) shell. Through ^{27}Al and ^{29}Si MAS NMR studies, we were able to elucidate the structural reasons behind the different deactivation (and stabilization) mechanisms of the model sorbents prepared. $(Al,Si)O_x$-stabilized sorbents contain various Al- and Si-containing phases, in particular calcium aluminosilicate glasses and Al-substituted belite (Al−Ca_2SiO_4). The presence of these metastable calcium aluminosilicate stabilizer phases correlates with a reduced degree of segregation, agglomeration, particle growth, and loss of CO_2-capture-active CaO when compared to the thermodynamically stable mixed oxide phases $Ca_3Al_2O_6$ and Ca_2SiO_4 that dominate in the sorbents that are stabilized by the respective single metal oxides. In other words, metastable calcium aluminosilicate (glasses) stabilize the core-shell-like morphology more efficiently, likely by decreasing the rates of formation, segregation and growth of the thermodynamically favored $Ca_3Al_2O_6$ and Ca_2SiO_4 phases, potentially due to slower diffusion of the constituting cations, retarding thereby the sintering of CaO particles and improving the sorbent's cyclic CO_2 uptake performance.

RESULTS AND DISCUSSION

Characterization of the Sorbents after Deposition of Metal Oxide Overcoats

ALD was applied to coat nanoparticles of $CaCO_3$ (Ca-NP, d_{avg} = 67 ± 15 nm) with shells of Al_2O_3, SiO_2, or mixtures thereof, i.e., $(Al,Si)O_x$ (Figure 1a). Specifically, we used trimethylaluminum (TMA) and bis(diethylamino)silane (BDEAS) as the ALD precursors for overcoats of Al_2O_3 and SiO_2. Furthermore, H_2O and O_3 were used as the hydrolyzing reagent and oxidant, respectively.[24,38] The number of ALD cycles (each ALD cycle contains several alternating pulses of the respective ALD precursor and H_2O or O_3, see Experimental Section for details) was varied between 4 and 60 cycles for sorbents with an alumina overcoat (denoted as Ca@Al) and between 30 and 90 cycles for sorbents with a silica overcoat (denoted as Ca@Si). In addition, sorbents stabilized by $(Al,Si)O_x$ overcoats, denoted Ca@$(Al,Si)O_x$, were synthesized by applying alternating layers of alumina and silica. Specifically, to prepare Ca@$(Al,Si)O_x$, we first applied 5 cycles of TMA/O_3 followed by 10 cycles of BDEAS/O_3 and repeated this TMA-BDEAS deposition sequence three times. The Al content in the as-prepared Ca@Al sorbents, as determined by inductively coupled plasma optical emission spectroscopy (ICP-OES), is presented in Table S3. The sorbents prepared using 4, 15, 30, and 60 ALD cycles of Al_2O_3, i.e., Ca@Al(4), Ca@Al(15), Ca@Al(30), and Ca@Al(60) have an Al_2O_3 weight content of 6.6, 11.5, 19.4, and 25.7 wt %, respectively. Thus, there is a clear trend between the number of ALD cycles (within the range of 4 to 60 cycles) and the weight of deposited Al (Figure S1a). Similarly, the SiO_2 weight content increased from 3.7 to 5.3 and 7.2 wt % for materials prepared using 30, 60, and 90 ALD cycles, i.e., Ca@Si(30), Ca@Si(60) and Ca@Si(90) (Figure S1b), while Ca@$(Al,Si)O_x$ contains 3.5 and 8.8 wt % of SiO_2 and Al_2O_3, respectively.

The XRD patterns of all of the as-prepared sorbents and the Ca-NP reference are shown in Figure 1b. For all sorbents, the patterns exhibit the characteristic diffraction peaks of the $CaCO_3$ polymorph calcite. Independent of the number of ALD cycles applied, no diffraction peaks relating to any crystalline phases of Al_2O_3 or any Ca−Al mixed oxide phase (e.g., $Ca_3Al_2O_6$ or $Ca_{12}Al_{14}O_{33}$) were observed for Ca@Al or Ca@$(Al,Si)O_x$. Similarly, no diffraction peaks due to crystalline SiO_2 or any mixed Ca−Si oxide (e.g., Ca_2SiO_4) phase are observed for Ca@Si or Ca@$(Al,Si)O_x$. Therefore, the deposited metal oxide overcoats were XRD-amorphous, which was confirmed by high-resolution TEM showing, e.g. that in Ca@$(Al,Si)O_x$ crystalline $CaCO_3$ nanoparticles are coated with an amorphous overcoat that is approximately 6−7 nm thick (Figure 1c,d). The successful preparation of an Al−Si overcoat and its homogeneity were further confirmed by EDX-TEM elemental mapping, demonstrating clearly a core−shell microstructure with a homogeneous distribution of Al and Si in the shell (Figure 1e−h). Furthermore, EDX-TEM characterization confirmed the fabrication of core−shell structures in representative sorbents containing a SiO_2, Ca@Si(60), or Al_2O_3, Ca@Al(15), shell, as shown in Figure S2. In addition, the Al 2*p* and Si 2*p* regions of the XPS spectra of as-prepared Ca@Al(30) and Ca@Si(60) showed the successful deposition of, respectively, Al-based or Si-based overcoats on the $CaCO_3$ NPs (Figure S3a,b).[39−41] For Ca@$(Al,Si)O_x$, both the Al 2*p* and Si 2*p* regions of the XPS spectrum exhibit peaks due to Al−O/Al−OH and Si−O/Si−OH, confirming the presence of

https://doi.org/10.1021/jacsau.3c00475
JACS Au 2023, 3, 3111−3126

Table 1. Comparison of the CO_2 Uptake and CaO Conversion Performance of Al_2O_3, SiO_2, and $(Al,Si)O_x$-Stabilized Sorbents[a]

sorbent	CaO content [wt %]	CO_2 uptake 1st cycle [g_{CO2} $g_{sorbent}^{-1}$]	CO_2 uptake 10th cycle [g_{CO2} $g_{sorbent}^{-1}$]	CO_2 uptake 10th cycle [g_{CO2} g_{CaO}^{-1}]	CaO conversion 10th cycle [%]
Ca-NP	>99	0.66	0.20	0.20	25.6
Ca@Al(15)	88.5	0.68	0.24	0.27	34.7
Ca@Al(30)	80.5	0.56	0.21	0.26	33.4
Ca@Al(60)	74.2	0.54	0.17	0.23	29.4
Ca@Si(30)	96.2	0.66	0.21	0.22	28.0
Ca@Si(60)	94.7	0.55	0.25	0.26	33.8
Ca@Si(90)	92.8	0.39	0.19	0.20	26.2
Ca@$(Al,Si)O_x$	87.7	0.57	0.31	0.35	45.3

[a]The CaO contents in the sorbents were determined by ICP-OES prior to their initial activation.

both Al and Si in the stabilizer overcoat in this material (Figure S3c,d). The Ca 2*p* regions of Ca@Al(30), Ca@Si(60), and Ca@$(Al,Si)O_x$ show the Ca $2p_{1/2}$ and Ca $2p_{3/2}$ peaks of $CaCO_3$ (calcite), indicating that, in general, the overcoat layers of the stabilizer phase(s) are thinner than the penetration depth of XPS, i.e. < ca. 10 nm (Figure S3e–g).[42,43] Notably, we did not observe any features in the N 1*s* XPS region of the as-prepared sorbents relating to the possible incorporation of nitrogen from the BDEAS precursor into the overcoat (Figure S4), nor any significant features in the C 1*s*, Al 2*p* or Si 2*p* region that would indicate the potential formation of carbides containing Al or Si or residual carbon, which is further confirmed by the absence of features relating to carbon in the Raman spectrum of the sorbent after the initial heat treatment (Ca@$(Al,Si)O_x$-0c, Figure S5a,b).

Characterization of the Sorbents after the Initial Heat Treatment in N_2

Before cyclic CO_2 capture experiments, the sorbents were activated by a heat treatment at 900 °C (heating ramp of 50 °C min^{-1}) for 5 min under a flow of N_2 (200 mL min^{-1}, ca. 30 ppm of O_2 in N_2), to transform $CaCO_3$ into CO_2-capture-active CaO. After the initial heat treatment, the respective materials are denoted as Ca@Al(*x*)-0c, Ca@Si(*x*)-0c, and Ca@$(Al,Si)O_x$-0c, where the notation 0c indicates that the materials were activated but not yet exposed to any carbonation-regeneration cycles. The XRD patterns of Ca@Al(*x*)-0c, Ca@Si(*x*)-0c and Ca@$(Al,Si)O_x$-0c are shown in Figure 1i. Diffraction peaks due to CaO and $Ca_3Al_2O_6$ were observed in all three activated sorbents of the Ca@Al-0c family. The relative intensity of the diffraction peaks of $Ca_3Al_2O_6$ increased notably with the number of ALD cycles. Rietveld refinement of the respective diffractograms yields 12 and 23 wt % $Ca_3Al_2O_6$ in Ca@Al(30)-0c and Ca@Al(60)-0c, respectively. Based on ICP-OES-determined Al-content, this implies that, respectively, 23 and 34% of the total quantity of Al_2O_3 deposited onto these sorbents is present in the form of crystalline $Ca_3Al_2O_6$ (Figure S6). Rietveld refinement of Ca@Al(15)-0c was not possible due to the broad and low-intensity Bragg diffraction peaks of $Ca_3Al_2O_6$ in this material. The formation of $Ca_3Al_2O_6$, i.e., the thermodynamically stable mixed phase between Al_2O_3 and CaO in the conditions applied here (650–900 °C) is in agreement with previous reports.[21,37,44] The crystallite size of CaO, determined via the Scherrer equation, was 34, 32, and 29 nm in Ca@Al(15)-0c, Ca@Al(30)-0c, and Ca@Al(60)-0c, respectively, revealing that there is only a minor dependency of the crystallite size of CaO on the Al content in Ca@Al. Yet it is worth noting that the sizes of the CaO crystallites in the Ca@Al-0c sorbents are significantly smaller than in the Ca-NP-0c reference (48 nm). Further, using the Scherrer equation, the crystallite size of $Ca_3Al_2O_6$ was estimated to be 32 and 36 nm in Ca@Al(30)-0c and Ca@Al(60)-0c, respectively. These crystallite sizes are larger than the initial overcoat thickness (<10 nm) in the respective as-prepared materials, consistent with the growth of the $Ca_3Al_2O_6$ phase during the initial activation step. For the Ca@Si sorbent family, XRD reveals only peaks due to CaO, while diffraction peaks due to any Ca–Si mixed oxides such as Ca_2SiO_4 were not observed (Figure 1i). Therefore, either the kinetics of the solid-state reaction between CaO and SiO_2 are slow (i.e., the amount of crystalline mixed oxide phases formed is smaller than the limit of detection of our XRD setup, <1 wt %) or the mixed oxide phases were XRD-amorphous. The crystallite size of CaO in the Ca@Si sorbents was in the range of 46–49 nm, which is close to the crystallite size of Ca-NP-0c (48 nm). For Ca@$(Al,Si)O_x$-0c, diffraction peaks of CaO and $Ca_3Al_2O_6$ were identified, and the crystallite size of CaO was 33 nm (a similar value as in the Ca@Al sorbents). Using Rietveld refinement, it was determined that Ca@$(Al,Si)O_x$-0c contained approximately 20 wt % of $Ca_3Al_2O_6$ (crystallite size of $Ca_3Al_2O_6$ of 29 nm, Figure S6c). The formation of a Ca–Al mixed oxide is conceivable as the first metal oxide layer deposited via ALD onto the $CaCO_3$ NPs is alumina. In a control experiment, changing the order of the metal oxide that is deposited first onto the $CaCO_3$ nanoparticles from Al_2O_3 to SiO_2 to reduce the formation of $Ca_3Al_2O_6$ did not have an appreciable effect on the CO_2 capture performance of the sorbent when compared to Ca@$(Al,Si)O_x$ (Figure S7), and therefore, this material will not be discussed further.

Turning now to the morphology of the overcoats after the initial heat treatment, Figure 1j–l shows a TEM micrograph and EDX-TEM elemental mappings of Ca, Al and Si in Ca@$(Al,Si)O_x$-0c. During the heat treatment, the CaO nanoparticles have sintered to larger agglomerates (Figure 1j) and the mixed $(Al,Si)O_x$ overcoat that initially covered the nanoparticles homogeneously has fragmented to some extent; however, Al and Si remained well-dispersed on the surface of the sorbent (Figure 1k,l). On the other hand, heat-treated Ca@Al(15)-0c exhibited Al-containing nanoparticles on the surface of CaO particles (Figure S2c), and also Ca@Si(60)-0c displayed a fragmented Si-containing overcoat (Figure S2d). As will be discussed in detail below, based on the Ca–Si–O phase diagram, the formation of Ca_2SiO_4 upon the initial heat treatment is expected in Ca@Si(60)-0c. Ca_2SiO_4 has a higher Tammann temperature (T_T = 873 °C) than $Ca_3Al_2O_6$ (T_T = 634 °C) that formed in Ca@Al, making a Ca_2SiO_4 overcoat potentially more sintering-resistant and allowing the sorbent to sustain its core–shell-like morphology after the initial heat treatment. To conclude, TEM and EDX revealed that the

https://doi.org/10.1021/jacsau.3c00475
JACS Au 2023, 3, 3111–3126

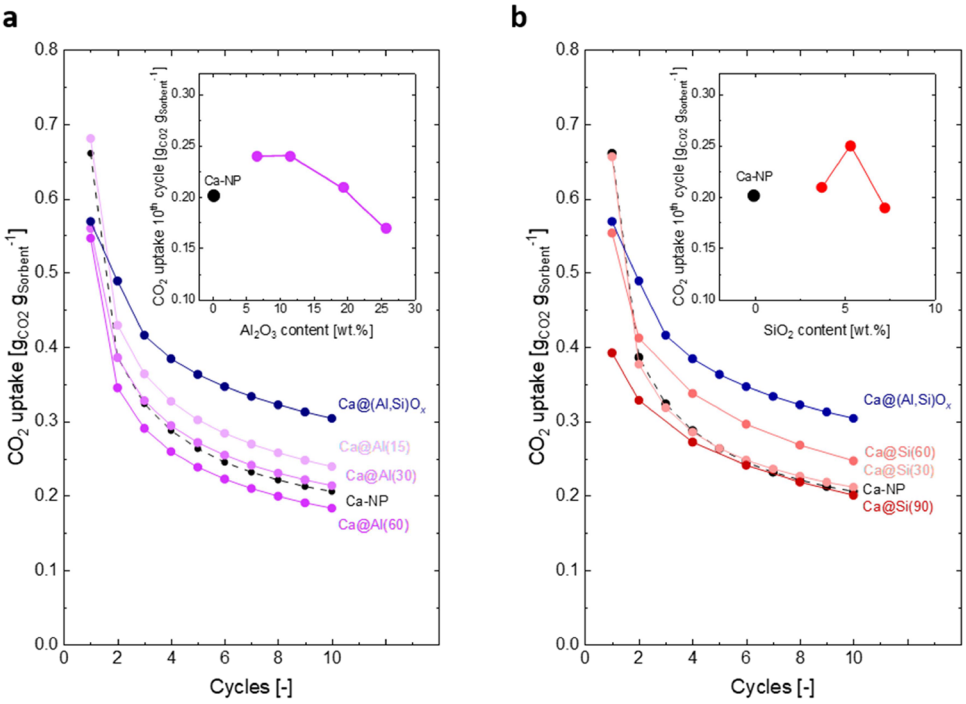

Figure 2. Cyclic CO_2 uptake over 10 consecutive carbonation-regeneration cycles of (a) Ca@Al, Ca-NP and Ca@(Al,Si)O_x and (b) Ca@Si, Ca-NP and Ca@(Al,Si)O_x. The insets show the CO_2 uptake in the 10th carbonation cycle as a function of the respective Al_2O_3 and SiO_2 contents in the sorbents, as determined by ICP-OES.

initial heat treatment transformed the as-prepared, homogeneous core−shell microstructure to fragmented particles of varying sizes on the surface of Ca@Al(15)-0c, while the core−shell-type microstructure was maintained to a larger extent (with some visible heterogeneity) in Ca@(Al,Si)O_x-0c and Ca@Si(60)-0c compared to Ca@Al(15)-0c.

Cyclic CO_2 Uptake Performance of the Sorbents

The cyclic CO_2 capture and release performance of Al_2O_3-, SiO_2-, and mixed (Al,Si)O_x-stabilized sorbents were evaluated under the following conditions: the as-prepared sorbents were first activated at 900 °C (5 min, 50 °C min^{-1}) in N_2 (200 mL min^{-1}), carbonated at 650 °C in 15 vol % CO_2 for 20 min and subsequently regenerated in 80 vol % CO_2 balanced with N_2 at 900 °C for 10 min. In the first cycle the reference material Ca-NP had a CO_2 uptake of 0.66 g_{CO2} $g_{sorbent}^{-1}$ (see also Table 1 for a comparison of the CO_2 uptakes in the first and 10th cycle of all of the materials tested), which is lower than the theoretical CO_2 uptake capacity of CaO (0.78 g_{CO2} $g_{sorbent}^{-1}$), implying only a partial conversion of CaO to $CaCO_3$ (~85%) at the given carbonation conditions.

In the 10th cycle, the CO_2 uptake of Ca-NP decreased by ca. 70% (compared to the first first cycle) to 0.20 g_{CO2} $g_{sorbent}^{-1}$ (Figure 2a). The cyclic CO_2 uptake of the Ca@Al sorbent family depended strongly on the alumina content (Figure 2a). While Ca@Al(4), Ca@Al(15), and Ca@Al(30) outperformed the Ca-NP benchmark in the 10th cycle by ca. 20, 20, and 5%, respectively (CO_2 uptake of, respectively, 0.24, 0.24, and 0.21 g_{CO2} $g_{sorbent}^{-1}$), Ca@Al(60) was a poor sorbent yielding a CO_2 uptake of only 0.17 g_{CO2} $g_{sorbent}^{-1}$ after 10 cycles. The poor CO_2 uptake of Ca@Al(60) is at least in part related to the high fraction of Al_2O_3 in this material (25.7 wt %) and, as a consequence, the formation of a large quantity of $Ca_3Al_2O_6$ (or other mixed oxides) that are inactive for CO_2 capture and an ineffective stabilizer against sintering due to segregation and agglomeration of the stabilizer phase. However, in the 10th cycle, the CaO conversion in all of the alumina-stabilized sorbents was higher than the CaO conversion achieved in the reference Ca-NP (Table 1). Turning to the Ca@Si family, the cyclic CO_2 uptake also showed a dependence on the fraction of Si in the material (Figure 2b). Here, the most promising sorbent, Ca@Si(60), yielded a CO_2 uptake of 0.25 g_{CO2} $g_{sorbent}^{-1}$ after 10 cycles (a 25% increase compared to Ca-NP). Interestingly, Ca@(Al,Si)O_x showed the lowest decay in the CO_2 uptake with cycling, yielding a CO_2 uptake of 0.31 g_{CO2} $g_{sorbent}^{-1}$ (>45% CaO conversion) after 10 cycles, viz. an increase of 55, 29, and 24% compared to Ca-NP and the most promising alumina-stabilized and silica-stabilized sorbents, Ca@Al(15) and Ca@Si(60), respectively (Table 1). The CO_2 uptake of Ca@(Al,Si)O_x after 10 cycles normalized by the CaO content is 0.35 g_{CO2} g_{CaO}^{-1}, which is higher than those of all other sorbents studied in this work. Importantly, also the cyclic CO_2 uptake of Ca@(Al,Si)O_x after 30 cycles was considerably higher (i.e., ca. 44%) than the cyclic CO_2 uptake of the benchmark Ca-NP (0.16 g_{CO2} g_{CaO}^{-1}, Figure S8). Note that previous reports focusing on the optimization of the structural and morphological properties of CaO-based sorbents yielded high and relatively stable cyclic CO_2 uptakes when MgO was used as a stabilizer. For example, multishelled, MgO-stabilized, CaO exhibited a CO_2 uptake of ca. 0.65 g_{CO2} $g_{Sorbent}^{-1}$ after 10 carbonation-regeneration cycles (conditions comparable to the present work),[31] and a CO_2 uptake of 0.44 g_{CO2} $g_{Sorbent}^{-1}$ after 50 cycles was reported for CaO stabilized with MgO via mechanical mixing.[45]

In summary, the mixed (Al,Si)O_x-stabilized sorbent Ca@(Al,Si)O_x notably outperformed the most promising single metal oxide-stabilized sorbents, i.e., Ca@Al(15) and Ca@Si(60), over consecutive carbonation-regeneration cycles. These differences in cyclic CO_2 uptake between the materials

https://doi.org/10.1021/jacsau.3c00475
JACS Au 2023, 3, 3111−3126

investigated here are based on differences in the CO_2 sorption rates of the sorbents in the first and 10th carbonation steps (see Figure S9). During the first carbonation step (650 °C, 15 vol % CO_2 in N_2, 20 min) Ca-NP and the sorbents that contain a single metal oxide overcoat, i.e. Ca@Si(30) and Ca@Al(15), exhibited first a fast, kinetically controlled regime of CO_2 sorption that is followed by a slower, diffusion-controlled regime (Figure S9). Such sorption kinetics are typical for CaO-based sorbents.[10,20,46] In these sorbents, the dominating part of the CO_2 uptake (>0.4 g_{CO2} g_{CaO}^{-1}) was achieved within the first 3 min, followed by a sharp transition to the slow diffusion-controlled regime. On the other hand, for Ca@(Al,Si)O_x, the transition between the two regimes is less abrupt and more gradual, and overall the rate of CO_2 sorption within the first 3 min was slower compared to the other sorbents. In the 10th carbonation step, Ca-NP, Ca@Al(15), and Ca@Si(30) again showed a clear transition between the two reaction regimes, whereas for Ca@(Al,Si)O_x the transition between the kinetically controlled and diffusion-controlled reaction regime was more gradual. Overall, the rate of CO_2 uptake was highest for Ca@(Al,Si)O_x (in particular in the diffusion-limited regime), resulting in a significantly higher total CO_2 uptake compared to the other sorbents. Thus, the carbonation rate as well as the transition behavior between the two regimes of the carbonation reaction are closely related to the structural (and morphological) properties of the sorbents.

Hence, to rationalize these findings, we turned to a detailed analysis to identify the differences in the morphological and structural characteristics of these sorbents.

Morphology of the Sorbents after Exposure to 10 Carbonation-Regeneration Cycles

First, we quantified the morphological parameters of key sorbents after 10 carbonation-regeneration cycles, compared them to the values after the initial heat treatment, and aimed to relate the differences observed with the sorbents' CO_2 uptake after 10 cycles. For our analysis, we selected the three most promising (by cyclic CO_2 uptake) sorbents for each type of stabilizer, i.e., Ca@Al(15), Ca@Si(60), and Ca@(Al,Si)O_x as well as the reference Ca-NP (Table 1, Figure 2).

Retaining a high surface area is arguably one of the most important morphological descriptors of CaO-based sorbents to sustain a high rate of CO_2 uptake.[9,47,48] Compared to the as-received commercial $CaCO_3$ nanoparticles (Ca-NP, S_{BET} = 15.6 m^2 g^{-1}), the deposition of an overcoat by ALD leads to a comparatively small reduction of the surface area of the materials, i.e., to 10.7, 12.4, and 12.5 m^2 g^{-1} for Ca@(Al,Si)O_x, Ca@Si(60) and Ca@Al(15) (Table 2). The SEM micrographs presented in Figure S10a–d show the as-prepared sorbents, which consist of small primary particles (<100 nm) that form larger agglomerates (several μm), with no significant differences between the sorbents. SEM analysis confirms that the deposition of metal oxide overcoats had no significant effect on the size and morphology of the $CaCO_3$ nanoparticles.

Table 2. BET Surface Area of Selected Sorbents at Different Stages Determined via N_2 Physisorption

	surface area [m^2 g^{-1}]		
sorbent	as-prepared	after initial heat treatment (0c)	after 10 cycles (10c)
Ca-NP	15.6	3.5	<2.5
Ca@Al(15)	12.5	4.6	<2.5
Ca@Si(60)	12.4	3.8	<2.5
Ca@(Al,Si)O_x	10.7	5.3	<2.5

On the other hand, the initial heat treatment in N_2 results in a more pronounced decrease in surface area. Ca@(Al,Si)O_x-0c (5.3 m^2 g^{-1}) features the highest surface area when compared to Ca@Al(15)-0c, Ca@Si(60)-0c and Ca-NP-0c (S_{BET} = 4.6, 3.8, and 3.5 m^2 g^{-1}, respectively). SEM micrographs of the sorbents after the initial heat treatment (Figure S10e–h) showed the smallest degree of sintering for Ca@(Al,Si)O_x, when compared with the other sorbents. After 10 carbonation-regeneration cycles, SEM (Figure S10i–l) confirms heavy sintering that is also reflected in surface areas <2.5 m^2 g^{-1} for all of the sorbents tested.

To further characterize the morphology (and changes thereof) of the sorbents, the materials were analyzed by TEM and EDX-TEM after their exposure to 10 carbonation-regeneration cycles. It is observed that Ca@Al(15)-10c is composed of sintered agglomerates (Figure 3a,b) that are notably larger than the CaO nanoparticles obtained after the initial heat treatment (Ca@Al(15)-0c, Figure S2). EDX-TEM also reveals the formation of Al-containing nanoparticles of ca. 100–150 nm in diameter located on the surface of the large Ca-rich agglomerates (Figure 3b,c). Selected area electron diffraction (SAED) (Figure 3d) on one of the segregated nanoparticles (Figure 3c) exhibits a single crystalline diffraction pattern consistent with the [3 0 0] (d = 2.56 Å), [3 0 3] (d = 1.78 Å), and [4 1 4] (d = 1.32 Å) planes of crystalline $Ca_3Al_2O_6$. Comparing the EDX-TEM maps of Ca@Al(15)-0c and Ca@Al(15)-10c, it can be concluded that with cycling there is an increasing degree of segregation of $Ca_3Al_2O_6$ (Figures 3a,b and S2e,f, respectively). During cycling, the $Ca_3Al_2O_6$ particles transformed from a relatively small size of <50 nm in Ca@Al(15)-0c to dendrite-shaped particles of >150 nm in length in Ca@Al(15)-10c (Figure S2e). The continuous formation of $Ca_3Al_2O_6$ (see ^{27}Al NMR section) with cycling leads to a loss of CO_2-capture-active CaO and growth of the $Ca_3Al_2O_6$ particles on the surface of CaO. Hence, the Ca@Al sorbents deactivate by a combination of a continuous reduction of the fraction of CaO (see below) and the formation of increasingly large and heterogeneously distributed $Ca_3Al_2O_6$ particles that are not effective in mitigating the sintering of CaO.[21] Furthermore, the dendritic shape of the $Ca_3Al_2O_6$ particles is consistent with the outward diffusion of Ca^{2+} ions into the Al_2O_3 overcoat.[49−51]

Turning now to the Ca@Si material family, Figure 3i,j shows, respectively, a TEM image and an EDX elemental map of Ca and Si in Ca@Si(60)-10c (regenerated state). Ca@Si(60)-10c is composed of sintered CaO particles with small Si-containing nanoparticles decorating their surface, i.e., the initially homogeneous Si-containing overcoat transformed into small, distributed nanoparticles during cycling. Due to the small size of these nanoparticles and their low TEM contrast when compared to CaO, we were not able to identify the respective phase via electron diffraction (^{29}Si MAS NMR was required for the phase identification as discussed in the following Section on ^{29}Si NMR).

With regard to CaO stabilized by a mixed oxide layer, it is noteworthy that the CaO nanoparticles in Ca@(Al,Si)O_x-10c have sintered to a lesser extent compared to Ca@Al(15)-10c and Ca@Si(60)-10c (Figure 3e–h). Although we cannot validate this inference by N_2 physisorption owing to the overall low surface area of the cycled materials (and given the low sample weight used in TGA experiments), it generally agrees

https://doi.org/10.1021/jacsau.3c00475
JACS Au 2023, 3, 3111−3126

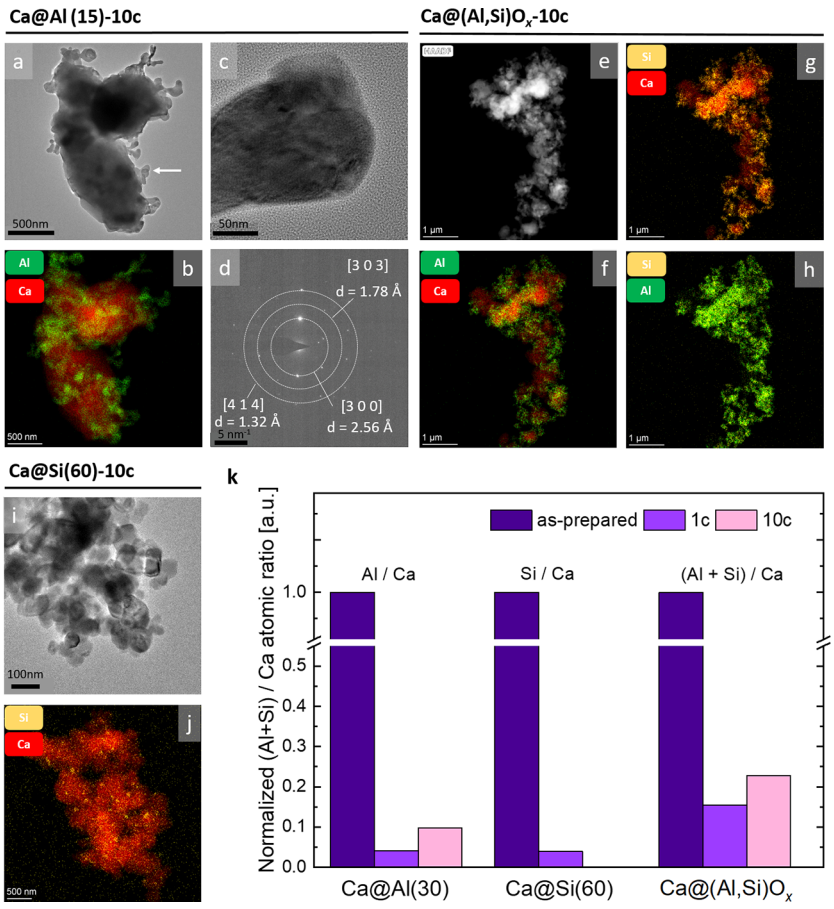

Figure 3. (a) TEM image and (b) EDX-TEM elemental mapping of Ca@Al(15)-10c (regenerated state), (c) high resolution TEM image and (d) SAED pattern of a nanoparticle on the surface of Ca@Al(15)-10c; (e) HAADF TEM image and (f–h) EDX-TEM elemental mapping (Ca, Al, Si) of Ca@(Al,Si)O_x-10c (regenerated state), (i) TEM image and (j) EDX-TEM elemental mapping (Ca, Si) of Ca@Si(60)-10c (regenerated state) and (k) (Al+Si) content normalized by the atomic ratio of the metal stabilizer(s) (Al, Si) to Ca after the 1st (1c) and 10th (10c) cycle obtained by fitting the XPS survey spectra.

with the observation of a slightly larger (by ca. >15%) surface area of Ca@(Al,Si)O_x-0c compared to Ca@Al(15)-0c and Ca@Si(60)-0c. Further, we observed a high dispersion of Al and Si on the surface of Ca@(Al,Si)O_x-10c, similar to that in Ca@(Al,Si)O_x-0c (Figure 1k,l), which notably contrasts the presence of distinct Al- or Si-containing nanoparticles in Ca@Al(15)-10c and Ca@Si(60)-10c, respectively. It is important to note that Al and Si-containing areas overlap in Ca@(Al,Si)O_x-10c (Figure 3h), consistent with the formation of Al−Si (or Ca−Al−Si) mixed oxides (see the Section on ^{27}Al NMR). Relating the morphological characteristics of the series of sorbents with their CO_2 sorption rate (Figure S9) it is found that sorbents that contain a single metal oxide overcoat (Ca@Al(15) and Ca@Si(30)) exhibited a less homogeneous coating of the CaO nanoparticle surface which results in a larger fraction of CaO being directly exposed to the gas atmosphere compared to Ca@(Al,Si)O_x, which exhibits a more homogeneous overcoat (even after cycling). These differences yield a very pronounced transition between the kinetically and diffusion-controlled reaction regimes for Ca@Al(15) and Ca@Si(30), whereas in Ca@(Al,Si)O_x the transition between the two reaction regimes is more gradual. This observation points to an earlier onset of the diffusion-limited stage of the carbonation reaction in materials in which a CaO core is covered by a homogeneous, yet CO_2-penetrable, metal oxide overcoat, which is more effective at stabilizing the sorbent against sintering. Nonetheless, in such materials, the apparent CO_2 uptake rate (and thus the rate of CO_2 diffusion through the overcoat) appears to be higher, leading in turn to higher CO_2 uptakes.

Next, we compared the (Al+Si)/Ca atomic ratios, obtained by XPS, in the near-surface layer of the as-prepared materials in the sorbents that have undergone one or ten carbonation-regeneration cycles (carbonated state). Normalizing the (Al+Si)/Ca atomic ratio in the as-prepared materials to unity, we observe a notable decrease of the Si/Ca ratio in Ca@Si(60) and the Al/Ca ratio in Ca@Al(30) over cycling, i.e., to 0.04 and 0.0 in the first and 10th carbonation-regeneration cycle for Ca@Si(60) and to 0.04 and 0.10 for Ca@Al(30) (Figure 3k). These results demonstrate the Ca content in the outer layer of the sorbents that is probed by XPS increased significantly. This is explained by the formation of Ca-containing mixed oxides near the surface and, likely, the fragmentation of the originally homogeneous stabilizing overcoat, leading to a surface exposure of Ca-containing phases. Unlike Ca@Al(30)-10c that retains surface Al, in Ca@Si(60)-10c, the surface Si content becomes negligible, yet surface Si is detected in Ca@Si(60)-1c, indicating that the process is gradual (Figure S11). In contrast, in Ca@(Al,Si)O_x a notably higher (Al+Si)/Ca ratio is observed, i.e., 0.15 and 0.23 for Ca@(Al,Si)O_x-1c and Ca@(Al,Si)O_x-10c, respectively. This appreciably higher stabilizer to Ca ratio in Ca@(Al,Si)O_x compared to Ca@Si

https://doi.org/10.1021/jacsau.3c00475
JACS Au 2023, 3, 3111−3126

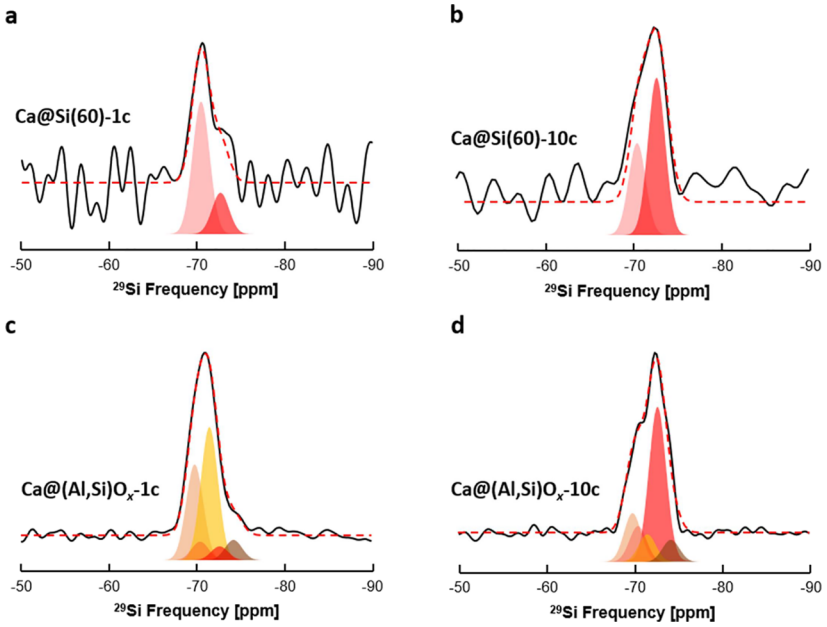

Figure 4. ^{29}Si CPMG MAS NMR experimental (black) and simulated (red) spectra acquired at 7.0 T for (a) Ca@Si(60)-1c, (b) Ca@Si(60)-10c, (c) Ca@(Al,Si)O_x-1c, and (d) Ca@(Al,Si)O_x-10c. The simulated data are shown in color, and the fitted values (isotropic chemical shift, relative fraction) are listed in Table 3. All spectra are recorded from materials in their carbonated state.

and Ca@Al correlates with an improved stabilization of the CO_2 uptake in Ca@(Al,Si)O_x. To summarize, XPS analysis provides evidence that the content of stabilizer phases at the surface of Ca@(Al,Si)O_x, i.e., the sorbent with the best cycling stability, is sustained to a larger degree during cycling compared to Ca@Al and Ca@Si sorbents, in line with the (EDX-)TEM data. In the following, we explore the element-specific local structure of the stabilizing phases and rationalize the differences in the cyclic CO_2 uptake performance of the sorbents discussed above from a (micro)structural point of view.

^{29}Si NMR Studies and Indication of Complex Phase Composition in Ca@(Al,Si)O_x

^{29}Si MAS NMR was used to investigate the local structure of the Si atoms in Ca@(Al,Si)O_x and Ca@Si(60). To this end, we studied sorbents after the first and 10th carbonation cycles (carbonated state). The carbonation conditions (20 min 15 vol % CO_2 balanced with N_2 at 650 °C) were chosen to limit the interaction of CaO with ambient humidity, which otherwise could lead to the formation of $Ca(OH)_2$ and hence a potential restructuring of the sorbent. ^{29}Si Carr−Purcell−Meiboom−Gill (CPMG) MAS NMR spectra were acquired for Ca@Si(60c)-1c and Ca@Si(60c)-10c and contrasted with those for Ca@(Al,Si)O_x-1c and Ca@(Al,Si)O_x-10c. We note that attaining a high signal-to-noise ratio in ^{29}Si spectra is challenging due to the relatively low content of Si in the studied materials (<8 wt % SiO_2, Table S3 and Figure S1b) that is further exacerbated by the low natural abundance of the isotope ^{29}Si (4.7%).[52] The recycle delay was optimized to ensure all potential sites can be observed in the spectra (see Figure S12).

The ^{29}Si CPMG MAS spectrum of Ca@Si(60)-1c displays resonances between ca. −69 and −75 ppm (Figure 4a) with the respective fitting parameters (δ_{iso}, % contribution) for these two peaks reported in Table 3.[53,54] Such downfield ^{29}Si resonances are commonly found in materials that contain SiO_4 tetrahedra with a low degree of condensation.[55] Therefore, the resonances in carbonated Ca@Si(60)-1c likely correspond to isolated SiO_4 tetrahedra (Q_0 sites) or two connected SiO_4 tetrahedra sharing one oxygen atom as the apex (Q_1 sites). Indeed, the deconvolution of the spectrum of Ca@Si(60)-1c revealed two unique ^{29}Si resonances at chemical shifts of $\delta_{iso}(^{29}Si)$ = −70.4 (major, ca. 76%) and −72.6 ppm (minor, ca. 24%, Figure 4a). These two peaks are indicative of an α-Ca_2SiO_4 phase, previously reported to have a $\delta_{iso}(^{29}Si)$ = −70.3 ppm,[54] and, in a likely minor amount, the respective hydroxide α-$Ca_2(SiO_3)(OH)_2$, $\delta_{iso}(^{29}Si)$ = −72.4 ppm.[56] The hydration-induced formation of α-$Ca_2(SiO_3)(OH)_2$ may have occurred during exposure of the sample to ambient conditions while handling the materials prior to the NMR experiment. At the high temperatures used for CO_2 capture and sorbent regeneration, only the Ca_2SiO_4 phase is expected to be present, which is in line with previous studies on SiO_2-stabilized CaO-based sorbents that have reported the formation of both α- and β-Ca_2SiO_4 polymorphs, depending on the applied temperature (the phase transformation from α to β polymorph occurs around 720−730 °C).[57,58] After 10 cycles, Ca@Si(60)-10c displays the same NMR features, i.e.

Table 3. ^{29}Si NMR Resonances Obtained by Fitting the Data of Ca@Si(60)-1c/10c and Ca@(Al,Si)O_x-1c/10c[a]

Assignment	δ_{iso} (ppm)	Relative fraction (%) 1c	10c
Ca@Si(60)			
α-Ca_2SiO_4	−70.4	76	37
α-$Ca_2(SiO_3)(OH)_2$	−72.6	24	63
Ca@(Al,Si)O_x			
Al-Sub β-Ca_2SiO_4	−69.8	34	16
α-Ca_2SiO_4	−70.4	7	4
β-Ca_2SiO_4	−71.5	47	9
α-$Ca_2(SiO_3)(OH)_2$	−72.6	5	54
	−74.2	7	7

[a]ΔCS (ppm) was set to 2.3 for all simulated features.

https://doi.org/10.1021/jacsau.3c00475
JACS Au 2023, 3, 3111−3126

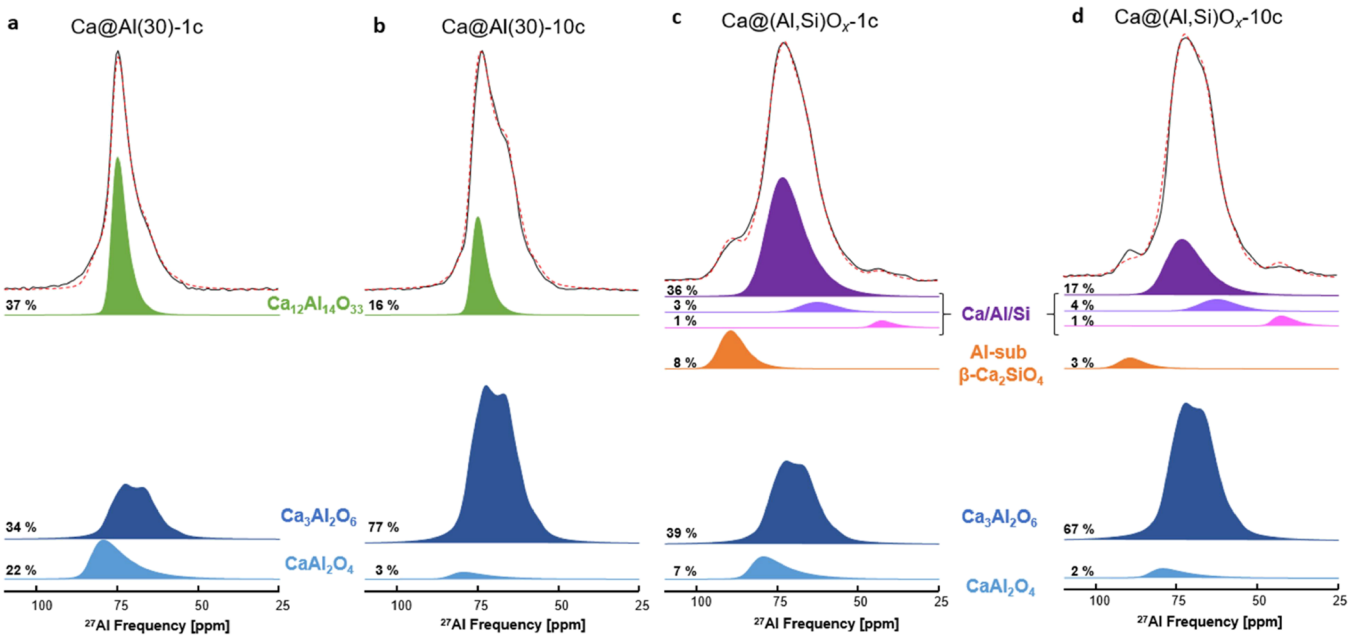

Figure 5. Quantitative 1D ^{27}Al MAS NMR experimental spectra (black) acquired at 20.0 T and simulated (dotted red) spectra of (a) Ca@Al(30)-1c, (b) Ca@Al(30)-10c, (c) Ca@(Al,Si)O_x-1c, and (d) Ca@(Al,Si)O_x-10c. The various components used to fit the experimental NMR spectra are shown in color, while the corresponding fitted NMR parameters are listed in Table 4. All spectra are recorded from materials in the carbonated state.

the two resonances due to α-Ca_2SiO_4 and α-$Ca_2(SiO_3)(OH)_2$ are observed, but their ratio changes from α-Ca_2SiO_4: α-$Ca_2(SiO_3)(OH)_2$ = 76:24 in Ca@Si(60)-1c to 37:63 in Ca@Si(60)-10c, indicating a larger degree of hydration in Ca@Si(60)-10c (Figure 4b), possibly due to reduced carbonate formation, acting as a protective layer, in the 10th carbonation cycle. Importantly, ^{29}Si MAS NMR does not show any resonances due to crystalline or amorphous SiO_2 phases (such as Q_4 sites with δ_{iso}(^{29}Si) in the range of −100 to −110 ppm). These NMR results suggest that the Si-containing nanoparticles in Ca@Si observed in our EDX-TEM analysis are composed of phase α-Ca_2SiO_4.

In contrast to the Ca@Si sorbent family, the ^{29}Si CPMG MAS spectrum of carbonated Ca@(Al,Si)O_x-1c exhibited a broader resonance (Figure 4c). Assuming the presence of α-Ca_2SiO_4 and α-$Ca_2(SiO_3)(OH)_2$ as in Ca@Si(60)-1c, we can use three additional peaks to fit the overall ^{29}Si signal. These three additional peaks constitute >88% of the total Si peak intensity of Ca@(Al,Si)O_x-1c and are located at δ_{iso}(^{29}Si) = −69.8, −71.5, −74.2 ppm, with a relative fraction of ca. 34, 47 and 7%, respectively (Figure 4c and Table 3). The peak at −71.5 ppm can tentatively be attributed to β-Ca_2SiO_4, whereas the downfield resonance at −69.8 ppm is attributed to SiO_4 tetrahedra in the vicinity of alumina species (see also discussion below) according to literature.[53,59] Importantly, the total relative fraction of these additional peaks decreases from ca. 88% in Ca@(Al,Si)O_x-1c to ca. 32% in Ca@(Al,Si)-O_x-10c, suggesting an evolution of the additional Si-containing species toward the α-Ca_2SiO_4 phase with increasing number of carbonation-regeneration cycles (Figure 4d).

Concerning the interpretation of the ^{29}Si MAS NMR data, the substitution of SiO_4 by AlO_4 in aluminosilicates typically leads to a downfield shift of δ_{iso}(^{29}Si), as observed here for Ca@(Al,Si)O_x-1c/10c, which suggests the formation of Al−Si mixed oxide phase(s) in Ca@(Al,Si)O_x and their gradual transformation to Ca_2SiO_4 during cycling.[52] Unfortunately, various (calcium) aluminosilicate phases can display resonances similar to the ones observed here, making a robust assignment of the exact phases present challenging when relying only on ^{29}Si NMR data. Therefore, to understand better the composition of the Al−Si mixed oxide phases in Ca@(Al,Si)O_x and their dynamics with cycle number, we performed complementary ^{27}Al MAS NMR experiments.

^{27}Al NMR Studies and Identification of Glassy Stabilizer Phases

^{27}Al solid-state MAS NMR spectroscopy has been instrumental for the identification of Al-containing species in a variety of inorganic materials ranging from cements to Ca−Al−Si mixed oxides (calcium aluminosilicates and their respective hydrates) and numerous other substituted or disordered materials.[60−63] In what follows, we describe the structural insight that was obtained from ^{27}Al MAS NMR studies of Ca@Al(30) and Ca@(Al,Si)O_x that have been exposed to either one or ten carbonation-regeneration cycles (as in the ^{29}Si NMR experiments, the sorbents were analyzed after the carbonation step).

Figure 5a,b presents quantitative 1D ^{27}Al MAS NMR spectra of Ca@Al(30)-1c and Ca@Al(30)-10c. Importantly, fitting the 1D and 2D spectra (presented in detail in Figures S13−16 in the Supporting Information) simultaneously allowed us to decipher accurately the complex phase composition of the materials. Ca@Al(30)-1c displays four unique Al resonances between 100 and 50 ppm and an additional weak resonance at $\overline{\delta}_{iso}$ (^{27}Al) = 12.1 ppm. The latter peak can be attributed to a hydrated six-coordinate aluminum (Al^{VI}) environment, likely resulting from the exposure of the sorbents to the humidity of air during handling. This assignment is consistent with ^{27}Al-{^{1}H}-D-HMQC experiments that confirm the close proximity between hydrogen and this specific Al^{VI} environment as well as the progressive increase of this resonance with an increased duration of the exposure of that sorbent to ambient conditions (Figure S17). Turning now to the resonances between 100 and

https://doi.org/10.1021/jacsau.3c00475
JACS Au 2023, 3, 3111−3126

Table 4. ^{27}Al NMR Parameters Based on the Fitting of the Respective Sorbents after the 1st and 10th Cycles (Carbonated States)[a]

Assignment	Color code	Site	δ_{iso} or $\bar{\delta}_{iso}$ (ppm)	C_Q* or $\bar{C}_Q$ (MHz)	η_Q* or ΔCS (ppm)	Relative fraction (%) 1c	10c
		Ca@Al(30)					
$Ca_3Al_2O_6$	Dark blue	Al^{IV}	79.7	8.8*	0.4*	34	77
$CaAl_2O_4$	Light blue	Al^{IV}	83.5	7.7	5.0	22	3
$Ca_{12}Al_{14}O_{33}$	Green	Al^{IV}	76.8	4.6	3.0	37	16
Hydrated species		Al^{VI}	12.1	3.3	6.1	7	4
		Ca@(Al,Si)O_x					
$Ca_3Al_2O_6$	Dark blue	Al^{IV}	79.7	8.8*	0.4*	39	67
Al-sub β-Ca_2SiO_4	Orange	Al^{IV}	92.6	5.5	6.4	8	3
$CaAl_2O_4$	Light blue	Al^{IV}	83.5	7.7	5.0	7	2
Ca/Al/Si	Dark purple	Al^{IV}	77.9	6.9	8.7	36	17
Ca/Al/Si	Light purple	Al^{IV}	66.5	5.9	10.0	3	4
Ca/Al/Si	Pink	Al^{V}	45.5	5.8	4.2	1	1
Hydrated species		Al^{VI}	12.1	3.3	6.1	6	6

[a] δ_{iso} , C_Q, and η_Q correspond to the isotropic chemical shift, the quadrupolar coupling constant and the quadrupolar asymmetric parameter, respectively, used for fitting a crystalline resonance. $\bar{\delta}_{iso}$, $\bar{C}_Q$, and ΔCS are the average isotropic chemical shift, the most probable quadrupolar coupling constant, and the chemical shift distribution used with the Czjzek model.

50 ppm, we observed three four-coordinated Al^{IV} environments with chemical shifts at δ_{iso} (^{27}Al) = 76.8, 79.7, and 83.5 ppm.[64] The two resonances at lower fields, i.e., at δ_{iso}(^{27}Al) = 76.8 and 79.7 ppm, can be attributed to Al sites in crystalline $Ca_{12}Al_{14}O_{33}$ and $Ca_3Al_2O_6$, respectively, whereas the resonance at δ_{iso}(^{27}Al) = 83.5 ppm is likely due to either crystalline $CaAl_2O_4$ or a glassy (i.e., likely amorphous) mixed CaO-Al_2O_3 oxide.[21,65,66] These assignments are in line with previous studies on the formation of both $Ca_{12}Al_{14}O_{33}$ and $Ca_3Al_2O_6$ in alumina-stabilized CaO-based sorbents using a combination of in situ XRD and dynamic nuclear polarization surface enhanced ^{27}Al NMR for their identification.[21] However, to the best of our knowledge, the formation of $CaAl_2O_4$ has not yet been observed in alumina-stabilized CaO-based sorbents. Note that both $CaAl_2O_4$ and $Ca_{12}Al_{14}O_{33}$ are metastable phases in the CaO-Al_2O_3 system at 900 °C, indicating that the structure of Ca@Al(30)-1c has not reached phase equilibrium.[44] Therefore, the dendritic structures that have been observed by TEM for Ca@Al(15)-10c (Figure 3a−d) could, in addition to crystalline $Ca_3Al_2O_6$ (identified also via SAED), also contain the poorly crystalline calcium aluminates observed by NMR.

With regard to the phase evolution in Ca@Al(30) with cycle number, fitting of the ^{27}Al MAS NMR spectrum of Ca@Al(30)-1c yields that $CaAl_2O_4$, $Ca_3Al_2O_6$ and $Ca_{12}Al_{14}O_{33}$ comprise, respectively, 22, 34 and 37% of all Al sites in this material (Table 4), while in Ca@Al(30)-10c 77% of Al sites are contained in crystalline $Ca_3Al_2O_6$, whereas (likely) amorphous $CaAl_2O_4$ and crystalline $Ca_{12}Al_{14}O_{33}$ contribute merely 3 and 16%, respectively. According to the phase diagram of the CaO-Al_2O_3 system, the phase equilibrium of Ca@Al(30) in the temperature range 650−900 °C is a mixture of CaO and $Ca_3Al_2O_6$.[67] Hence, the results of our 1D ^{27}Al MAS NMR experiments are in agreement with phase equilibrium arguments in that the metastable $CaAl_2O_4$ and $Ca_{12}Al_{14}O_{33}$ phases transform to $Ca_3Al_2O_6$ over repeated carbonation-regeneration cycles (which is also in general agreement with the XRD and TEM analyses discussed above). Comparing the Ca:Al ratios in these phases, the transformation of metastable $CaAl_2O_4$ (Ca:Al = 0.5) and $Ca_{12}Al_{14}O_{33}$ (Ca:Al = 0.86) to $Ca_3Al_2O_6$ (Ca:Al = 1.5) leads to a loss of reactive CaO as the Ca content per stabilizer atom (Al) in the mixed oxide phase increases. Taking also into account the CO_2 uptake performance of the Ca@Al sorbents, we conclude that (i) surface-segregated particles of $Ca_3Al_2O_6$ are ineffective in preventing the sintering of CaO/$CaCO_3$, and (ii) the increasing relative fraction of $Ca_3Al_2O_6$ leads to a decreasing amount of CaO available for reaction with CO_2 (see Figure 2 and discussion below).[9,20,68]

Turning now to the material containing an (Al,Si)O_x overcoat, the ^{27}Al MAS NMR spectrum of Ca@(Al,Si)O_x-1c (carbonated state) exhibited six resonances between 100 and 50 ppm as well as the previously discussed Al^{VI} environment at $\bar{\delta}_{iso}$(^{27}Al) = 12.1 ppm (Figure 5c). In Ca@(Al,Si)O_x-1c crystalline $Ca_3Al_2O_6$ (δ_{iso}(^{27}Al) = 79.7 ppm) and $CaAl_2O_4$ (δ_{iso}(^{27}Al) = 83.5 ppm) comprise, respectively, 39 and 7% of all of the Al sites in the material. Noteworthy, the Al site due to $Ca_{12}Al_{14}O_{33}$ was not observed in Ca@(Al,Si)O_x-1c. When compared to Ca@Al(30), four additional resonances are present in the spectrum of Ca@(Al,Si)O_x-1c. These resonances feature $\bar{\delta}_{iso}$(^{27}Al) = 77.9, 92.6, 66.5, and 45.5 ppm and contain 36, 8, 3, and 1% of all of the Al sites in the material, respectively (Table 4). The resonances below 80 ppm can be attributed to glassy calcium aluminosilicate phases of varying composition (mixed phases of CaO/SiO_2/Al_2O_3, see below) that account for ca. 40% of all of the Al sites.[69] The 2D ^{27}Al-MQMAS spectra provided further evidence for the presence of such additional calcium aluminosilicate phases in Ca@(Al,Si)O_x and their absence in Ca@Al(30) (see Figures S13−16). The presence of calcium aluminosilicate phases in Ca@(Al,Si)O_x-1c and Ca@(Al,Si)O_x-10c is consistent with our ^{29}Si NMR analysis, as discussed previously.

To further elucidate the formation of calcium aluminosilicate phases, 1D dipolar-based ^{29}Si−^{27}Al heteronuclear NMR sequence experiments were conducted for Ca@(Al,Si)O_x-1c (Figure 6, the sequence was optimized in previous reports for the calcium aluminosilicate anorthite).[70] Two different recoupling times were used (τ_{rec} = 3.2 and 6.4 ms). With varying recoupling times, we can assess the Al−Si interactions at different distances from the central Al site, i.e., an increasing recoupling time allows us to assess contributions from larger distances. The obtained spectra clearly display the presence of

https://doi.org/10.1021/jacsau.3c00475
JACS Au 2023, 3, 3111−3126

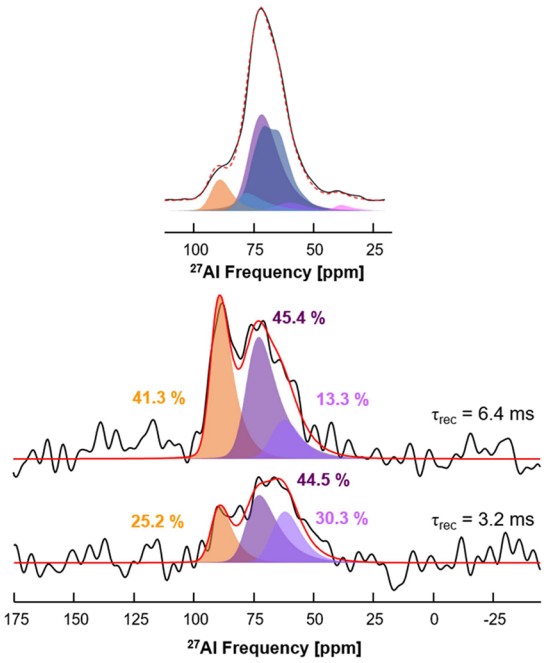

Figure 6. $^{27}Al\{^{29}Si\}$ 1D D-HMQC $SR4_1^2$ MAS NMR spectra of Ca@(Al,Si)O_x-1c acquired at 17.6 T for two recoupling times, τ_{rec}, of 3.2 and 6.4 ms. The fitting of the orange and purple components relies on the NMR parameters used for the quantitative fitting of the 1D ^{27}Al MAS spectra. Atop are the experimental (black) and simulated (red) ^{27}Al one pulse quantitative MAS spectra of Ca@(Al,Si)O_x-1c.

AlO_4 tetrahedra in the vicinity of SiO_4 tetrahedra, confirming that Al^{IV} environments with simulated chemical shifts at $\overline{\delta}_{iso}(^{27}Al)$ = 66.5, 77.9, and 92.6 ppm are close to Si atoms, very likely through a shared oxygen atom. Such a close vicinity of Al^{IV} and Si atoms is expected in calcium aluminosilicate phases. It is important to reiterate that the three ^{27}Al resonances recorded here are only observed in Ca@(Al,Si)O_x-1c but do not appear in Ca@Al(30)-1c (Tables 3 and 4), which is in line with our assignment of resonances at $\overline{\delta}_{iso}(^{27}Al)$ = 66.5, 77.9, and 92.6 ppm to calcium aluminosilicates. The "Czjzek" line shape for those three resonances also shows that they belong to disordered phases, likely glasses, which hence are very difficult to evidence using X-ray diffraction techniques. Notably, compared to the material after the initial heat treatment (Ca@(Al,Si)O_x-0c), the XRD pattern of Ca@(Al,Si)O_x-10c, i.e., the respective sorbent after 10 cycles (regenerated state) shows an increase in the crystallite size of $Ca_3Al_2O_6$ (i.e., a crystallite size of 47 nm as estimated from the Scherrer equation compared to 29 nm after the initial heat treatment, Figure S18). Yet, the other metal oxide phases in the cycled sorbent, such as Ca_2SiO_4, are not clearly identifiable by XRD, due to either their small quantities or amorphous nature.

In Ca@(Al,Si)O_x-1c, the relative fraction of the calcium aluminosilicate phase(s) totaled approximately 48% of all of the Al sites in the material (Table 4). With carbonation-regeneration cycles, the Al-containing phases transform into the thermodynamically stable $Ca_3Al_2O_6$ phase, the fraction of which increases from 39% in Ca@(Al,Si)O_x-1c to 67% in Ca@(Al,Si)O_x-10c while simultaneously the fraction of the calcium aluminosilicate phase with $\overline{\delta}_{iso}(^{27}Al)$ = 77.9 ppm decreased to 17% (from 36% in Ca@(Al,Si)O_x-1c). Furthermore, the relative fraction of the calcium aluminosilicate species with a resonance at $\overline{\delta}_{iso}(^{27}Al)$ = 92.6 ppm decreases to 3% in Ca@(Al,Si)O_x-10c (from 8% in Ca@(Al,Si)O_x-1c), such that only about 24% of the Al is found in calcium aluminosilicates in Ca@(Al,Si)O_x-10c. Therefore, while a complex mixture of phases is present both in Ca@(Al,Si)O_x-1c and Ca@(Al,Si)O_x-10c, the phase composition evolves toward higher fractions of the thermodynamically stable phases of $Ca_3Al_2O_6$ and Ca_2SiO_4 during cycling (see our ^{29}Si NMR results in Figure 4).[71]

Having established the presence of resonances due to calcium aluminosilicates in both the ^{29}Si and ^{27}Al NMR spectra of Ca@(Al,Si)O_x, and relating the presence of these two phases to an improved morphological and CO_2 capture performance stabilization, we endeavored to identify the specific calcium aluminosilicate phases present. Based on previous works, several calcium aluminosilicate glasses exhibit resonances in ^{27}Al NMR similar to the ones observed here.[69] For example, it was reported that the CA12.44 glass (12 mol % SiO_2, 44 mol % Al_2O_3 and 44 mol % CaO) displays signals for Al^{IV} at $\delta_{iso}(^{27}Al)$ = 77.9 ppm ($\overline{C}_Q$ = 6.6 MHz and ΔCS = 10.3 ppm) and for Al^V at 44.2 ppm ($\overline{C}_Q$ = 5.3 MHz and ΔCS = 10.0 ppm).[69] These resonances are very close to those observed for Ca@(Al,Si)O_x (Al^{IV} at $\overline{\delta}_{iso}(^{27}Al)$ = 77.9 ppm and Al^V at 45.5 ppm). In addition, a Ca50.40 phase (i.e., 40 mol % SiO_2, 10 mol % Al_2O_3, and 50 mol % CaO) with $\overline{\delta}_{iso}(^{27}Al)$ = 66.5 ppm has been reported, which coincides with the AlO_4 resonance we observe for Ca@(Al,Si)O_x. These NMR signatures confirm that glasslike calcium aluminosilicates are formed in Ca@(Al,Si)O_x and such glasses contribute to approximately 40% of all of the Al sites in Ca@(Al,Si)O_x-1c. Interestingly, previous computational studies suggested that the self-diffusion coefficients of Ca, Al, and Si in calcium aluminosilicate glasses (at temperatures above 1000 °C) depend on the relative Si and Al contents, e.g., in glasses with a high Al content (close to a Ca−Al mixed oxide), the self-diffusion coefficients decrease with an increase in the Si content.[72,73] Notably, the self-diffusion coefficients already decrease significantly when small amounts of Si or Al are present in an Al-rich or Si-rich glass. Based on these findings, it can be argued that the improved morphological and CO_2 uptake stability in Ca@(Al,Si)O_x (when compared to Ca@Si and Ca@Al) is due to lower self-diffusion coefficients in such glasses leading in turn to a reduced degree of phase segregation, surface restructuring, and sintering/agglomeration. Yet these stabilizing effects become weaker due to a gradual phase transition to the thermodynamically favorable phases ($Ca_3Al_2O_6$ and Ca_2SiO_4) with cycling.

Resonances of Al^{IV} environments rarely exceed 90 ppm, yet here we observed an Al^{IV} resonance at $\overline{\delta}_{iso}(^{27}Al)$ = 92.6 ppm. It has been reported that an Al^{IV} resonance in an Al-substituted belite material (β-Ca_2SiO_4 with Si positions substituted by Al) resides at $\overline{\delta}_{iso}(^{27}Al)$ = 96.1 ppm.[74] The presence of such an AlO_4-substituted Ca_2SiO_4 material agrees with our ^{29}Si NMR results for Ca@(Al,Si)O_x (Figure 4), wherein a higher chemical shift results from shorter Al−O bond lengths (Al−O = 1.61−1.65 Å) in the crystal lattice of belite compared to most calcium aluminates (Al−O = 1.73−1.81 Å).[74] Therefore, we attribute the feature at $\overline{\delta}_{iso}(^{27}Al)$ = 92.6 ppm to AlO_4 species in the vicinity of SiO_4 tetrahedra in a Al-substituted belite. The decrease of the relative fraction of AlO_4-substituted Ca_2SiO_4 with cycling is also in line with our ^{29}Si NMR data, indicating that this phase is metastable at our operating conditions and it transforms to $Ca_3Al_2O_6$. Similarly, the decrease of Al sites in calcium aluminosilicates with cycling is

https://doi.org/10.1021/jacsau.3c00475
JACS Au 2023, 3, 3111−3126

paralleled by an increase of Si sites in α-Ca_2SiO_4 with cycle number, as observed by ^{29}Si NMR.

Using the NMR-derived phase composition of the sorbents, we can now quantify the loss of CO_2-active CaO due to its interaction with the stabilizer phases. To this end, we calculate the Ca:(Al+Si) ratios of the stabilizer phases in a specific sorbent (evidenced by NMR) and weigh their contribution by the total amount of Al and Si sites in the material. Specifically, the Ca content in the stabilizer phases in Ca@Al(30)-1c and Ca@Al(30)-10c increases from 0.94 to 1.31 (Ca:Al), indicative of an appreciable loss of CO_2 capture-active CaO during cycling owing to the formation of calcium aluminates with a higher relative Ca content (e.g., $Ca_3Al_2O_6$ compared to $CaAl_2O_4$). For Ca@Si(60)-1c and Ca@Si(60)-10c, the Ca content in the mixed oxide stabilizer phases is constant during cycling, viz. Ca:Si = 2.0, as only Ca_2SiO_4 (and the respective hydrate) are formed. The complex phase composition in Ca@(Al,Si)O_x leads to a reduced Ca content in the stabilizer phases, i.e., Ca:(Al+Si) = 0.98 and 1.19 in Ca@(Al,Si)O_x-1c and Ca@(Al,Si)O_x-10c, respectively. In Ca@(Al,Si)O_x the quantity of CO_2-capture-active CaO decreases with cycling, but after 10 cycles the relative content of Ca in the respective stabilizer phases in Ca@(Al,Si)O_x remains lower than in Ca@Al(30) and Ca@Si(60), leading to a reduced loss of CO_2-capture-active CaO during cycling compared to the other sorbents. Hence, the superior stability of the cyclic CO_2 uptake of Ca@(Al,Si)O_x can be explained by both an improved stabilization of the overcoat and the morphology of the sorbent, leading to a reduction of the loss of CO_2-capture-active CaO during the phase transformation of the stabilizing phases. These results highlight the potential of an unexplored material design route, i.e., the design of (glassy) stabilizer phases with low self-diffusion coefficients, thermodynamic stability, and low Ca content.

CONCLUSIONS

In this work, we compared the stabilization of the cyclic CO_2 uptake of CaO-based sorbents that were coated via ALD with an overcoat of Al_2O_3, SiO_2 or a mixed (Al,Si)O_x overcoat. While the Al_2O_3- and SiO_2-stabilized sorbents outperformed the cyclic CO_2 uptake of the unstabilized CaO nanoparticle benchmark by ca. 25% (after 10 carbonation-regeneration cycles), the cyclic stability of the (Al,Si)O_x-stabilized sorbent showed a ca. 50% improvement compared to the CaO benchmark.

Using ^{27}Al NMR, we show that Al_2O_3-stabilized CaO nanoparticles initially contain the phases $Ca_3Al_2O_6$, $CaAl_2O_4$ and $Ca_{12}Al_{14}O_{33}$, yet with cycling, the thermodynamically favored $Ca_3Al_2O_6$ phase becomes dominant. Increasing the number of CO_2 capture-regeneration cycles further, the formation of large dendritic structures of $Ca_3Al_2O_6$ at the surface of CaO particles is observed. Such structures are ineffective in preventing the sintering of CaO and hence lead to a decreasing cyclic CO_2 uptake (in combination with the formation of Ca-richer, CO_2-capture-inactive stabilizing phases during cycling).

^{29}Si NMR reveals that the SiO_2-stabilized sorbents contain dispersed Ca_2SiO_4 nanoparticles rather than dendritic structures, yet also in this material, appreciable sintering of CaO was observed. Both Al_2O_3 and SiO_2-stabilized sorbents lose their initial core−shell morphology due to the fragmentation of the stabilizing film during cycling, preventing an effective stabilization of the CaO nanoparticle morphology.

Sorbents stabilized by mixed (Al,Si)O_x overcoats showed the highest cyclic stability among all sorbents tested and this is attributed to a complex, nonequilibrium composition of mixed oxides, specifically the presence of calcium aluminosilicate glasses and Al-substituted belite (Ca_2SiO_4) in addition to low amounts of Ca−Al and Ca−Si mixed oxides. This complex phase composition prevented the formation of segregated surface nanoparticles and/or dendritic structures, likely due to the lower diffusion coefficients of Ca, Al and Si in calcium aluminosilicate glasses, which reduces the mobility of the stabilizer phases and their migration. Thus, a homogeneous distribution of the stabilizing phase is maintained in Ca@(Al,Si)O_x to a larger extent when compared to Ca@Al and Ca@Si, leading to a lower degree of sintering and hence the initial CaO morphology is conserved to a larger extent as well. In addition, the complex phase composition of the stabilizing phases in Ca@(Al,Si)O_x led to a reduced loss of CO_2-capture-active CaO when compared to that of Ca@Al and Ca@Si sorbents, further contributing to its improved CO_2 capture performance. Nonetheless, the phase composition and therefore also the stabilizing effect is currently kinetic in nature, that is, the phase composition in Ca@(Al,Si)O_x also evolved with cycling toward the thermodynamic equilibrium composition (i.e., a mixture of $Ca_3Al_2O_6$, Ca_2SiO_4, CaO), which is associated with segregated stabilizer phases and the sintering of CaO.

MATERIALS AND METHODS

Atomic Layer Deposition

The deposition of Al_2O_3 and SiO_2 overcoats onto $CaCO_3$ nanoparticles (≥97.5%, SkySpring Nanomaterials, used as received) was performed in a commercial atomic layer deposition setup (Sunale R200, Picosun) using 200 mg of $CaCO_3$ nanoparticles for deposition. To grow Al_2O_3 overcoats, trimethylaluminum (TMA, Strem Chemicals, min 98%) was used as the Al precursor (source temperature of 25 °C) and deionized water to hydrolyze the deposited Al-based species. In a typical deposition process, 5 pulses of TMA (0.15 s, 15 s purge with N_2) were followed by 5 pulses of DI water (0.15 s, 15 s purge with N_2) at a reaction chamber temperature of 300 °C for up to 60 deposition cycles, yielding a deposition rate of ∼1 Å per cycle.[24,37] For the growth of SiO_2 films, bis(diethylamino)-silane (BDEAS, Strem Chemicals, 97%) was used as the precursor (source temperature 60 °C). During deposition, 5 pulses of BDEAS (0.4 s, 15 s purge with N_2) were followed by 5 pulses of ozone (0.2 s, 15 s purge with N_2) at a chamber temperature of 200 °C for up to 90 cycles.[75,76] For the mixed Al_2O_3−SiO_2-stabilized sorbents, injections of TMA and BDEAS were alternated 3 times (TMA/ozone: 5 cycles, 5 pulses per cycle, 0.15 s TMA, 0.2 s ozone, 15 s purge with N_2; BDEAS/ozone: 10 cycles, 5 pulses per cycle, 0.4 s BDEAS, 0.2 s ozone, 15 s purge with N_2). After the deposition, the materials were stored in glass vials sealed with paraffin.

Powder X-ray Diffraction (XRD)

Powder XRD analysis was conducted on a PANalytical Empyrean diffractometer using Cu K_α radiation with a wavelength of λ = 1.5418 Å. Measurements were carried out in the 2θ range of 5−90° with a step size of 0.0016°, resulting in a measurement time of approximately 60 min per sample. Before the measurement, the materials (∼10 mg) were placed on zero-background holders. Rietveld refinement was performed using the FullProf Suite software.[77]

Electron Microscopy

The morphology and the elemental distribution within the prepared sorbents were analyzed via an FEI Talos F200X microscope operating in scanning transmission electron microscopy (STEM) mode using an operating voltage of 200 kV. For compositional analysis, a large collection-angle energy-dispersive X-ray (EDX) detector was used.

https://doi.org/10.1021/jacsau.3c00475
JACS Au 2023, 3, 3111−3126

Before the measurement, the sorbents were deposited onto a carbon-coated Cu grid.

Thermogravimetric Analysis (TGA)

The initial heat treatment and cyclic CO_2 uptake experiments were conducted in a thermogravimetric analyzer (DSC 3+, Mettler Toledo). For the initial heat treatment, ca. 10 mg of material was placed in a Pt crucible (70 μL) and heated to 900 °C with a heating ramp of 50 °C min^{-1} under a 200 mL min^{-1} flow of N_2. After holding for 10 min at 900 °C, the specimen was cooled down to 25 °C (50 °C min^{-1}, 200 mL min^{-1} N_2), recovered, and stored in a sealed glass vial. For cyclic CO_2 uptake experiments, ca. 10 mg of the specimen was placed in a Pt crucible and activated as described above. Subsequently, the specimen was cooled down to 650 °C and carbonated in 15 vol % CO_2 (balanced with N_2, total flow rate of 200 mL min^{-1}) for 20 min. The carbonated material was then regenerated at 900 °C for 10 min in 80 vol % CO_2 balanced with N_2.[78] These carbonation-regeneration cycles were repeated up to 30 times. The cyclic CO_2 uptake (C_{CO_2}) in each cycle was calculated according to eq 1, where $m_{carb,i}$ is the specimen mass at the end of the ith carbonation step and m_{act} is the mass of the specimen after the initial heat treatment in N_2.

$$C_{CO_2} = \frac{m_{carb,i} - m_{act}}{m_{act}} \quad (1)$$

N_2 Physisorption

Nitrogen physisorption experiments were conducted using a Nova 800 analyzer (Anton Paar). Before the physisorption experiment, the materials (~100 mg) were outgassed for 3 h at 300 °C. N_2 adsorption and desorption were performed at −196 °C using liquid nitrogen cooling, and the surface area was determined using the Brunauer−Emmett−Teller (BET) model using the Kaomi software package provided by Anton Paar.

^{27}Al MAS NMR

Experiments were performed on Bruker 750 Avance III (17.6 T) and Bruker 850 Avance NEO (20.0 T) spectrometers operating at ^{27}Al Larmor frequencies of 195.4 and 221.5 MHz, respectively. Materials were packed in 2.5 mm zirconia rotors and spun at 33.3 kHz using double-resonance probes on both spectrometers. All spectra were referenced with respect to a 1 M solution of $Al(NO_3)_3$ and to tetramethylsilane (TMS) for ^{1}H. Quantitative 1D spectra were recorded by using a flip angle of less than $\pi/18$, i.e., with an excitation pulse length of 0.5 μs (radio frequency field ν_{RF} = 50 kHz).[79] Recycle delays (0.015 × T_1) were chosen after estimation of the longest spin−lattice relaxation time T_1 (~500 ms) using a saturation-recovery experiment on the most sensitive sample (i.e., Ca@Al(30)). All experimental NMR parameters are presented in Table S1 and 1D and 2D simulations were performed using the Dmfit software after baseline correction using an iterative baseline correction algorithm.[80,81] The Gaussian isotropic model (GIM − Czjzek, d = 5) was used for most of the ^{27}Al resonances.[38] Double-resonance ^{27}Al{1H} and ^{27}Al{^{29}Si} D-HMQC experiments were performed at 17.6 T using 2.5- and 4-mm probes spinning at 33.3 and 15.0 kHz, respectively, and applying $SR4_1^2$ recoupling schemes; see Table S1 for more details. Double-frequency sweeps (DFS) were used for both experiments.[82,83]

^{29}Si MAS NMR

CPMG experiments were carried out on a Bruker Avance 300 spectrometer (7.0 T) operating at a ^{29}Si Larmor frequency of 59.6 MHz using a 4 mm Bruker MAS probe. A recycle delay of 10 s and a spinning speed of 10 kHz have been used for all ^{29}Si experiments, and chemical shifts are referenced to TMS at 0 ppm. All relevant experimental NMR parameters are summarized in Table S2.

Inductively Coupled Plasma Optical Emissions Spectroscopy (ICP-OES)

ICP-OES (Agilent 5100 VDV) was used to determine the Ca and Al contents in the sorbents. The specimens were dissolved in aqua regia prior to their characterization. The Si content in the sorbents was assessed by the Pascher Mikroanalytik Laboratory (Germany).

X-ray Photoelectron Spectroscopy (XPS)

XPS analysis was conducted using a PHI Quantera SXM (ULVAC-PHI, Chanhassen, MN, USA) equipped with a monochromatic Al Kalpha source (1486.6 eV) and a beam diameter of 200 μm. The analyzer worked in constant-analyzer-energy (CAE) mode, and for the acquisition of survey spectra a pass energy of 280 eV, a step time of 20 ms, and a step size of 1.0 eV was used. Narrow scans in high resolution were acquired with a lower pass energy of 55 eV and a step size of 0.1 eV. For all experiments, a low-voltage argon ion gun/electron neutralizer was used. For calibration, the high-resolution spectra were calibrated using Au 4f7/2 at 84.0 eV with gold foil and subsequently using the C 1s peak at 248.8 eV of surface adventitious carbon species (C−C, sp^3) in every sample. The spectra were fitted by using the software package CasaXPS version 2.3.25PR1.0. Subtraction of the background was performed according to Shirley whereby atomic sensitivity factors according to Scofield were used to estimate the atomic composition.[84,85] The ratios of the metal oxide stabilizer phases to the Ca-containing phases in the surface layer were derived by fitting the areas under the respective peaks in the survey spectra of the as-prepared and cycled sorbents.

Fourier-Transform Infrared Spectroscopy (FTIR)

Fourier-transform infrared spectroscopy was conducted using an Alpha II spectrometer (Bruker) in a MBraun glovebox with H_2O and O_2 levels <1 ppm using self-supported pellets.

Raman Spectroscopy

Measurements were performed at room temperature using a 455 nm excitation laser (full range grating, 100−3500 cm^{-1}, 1200 lines per millimeter) on a DRX 2 Raman microscope (Thermo Fischer).

■ ASSOCIATED CONTENT

Data Availability Statement

All data of the main manuscript will be deposited into a public data repository.

Supporting Information

The Supporting Information is available free of charge at https://pubs.acs.org/doi/10.1021/jacsau.3c00475.

Details on NMR experimental conditions and results, ICP-OES, EDX-TEM, FTIR, Raman spectroscopy, cyclic assessment, SEM, and XRD (PDF)

■ AUTHOR INFORMATION

Corresponding Authors

Alexey Fedorov − *Department of Mechanical and Process Engineering, ETH Zurich, 8092 Zurich, Switzerland;* orcid.org/0000-0001-9814-6726; Email: fedoroal@ethz.ch

Pierre Florian − *CNRS, CEMHTI UPR3079, Orléans 45071, France;* orcid.org/0000-0003-4306-0815; Email: pierre.florian@cnrs-orleans.fr

Christoph R. Müller − *Department of Mechanical and Process Engineering, ETH Zurich, 8092 Zurich, Switzerland;* orcid.org/0000-0003-2234-6902; Email: muelchri@ethz.ch

Authors

Maximilian Krödel − *Department of Mechanical and Process Engineering, ETH Zurich, 8092 Zurich, Switzerland;* orcid.org/0000-0002-8230-9719

César Leroy − *CNRS, CEMHTI UPR3079, Orléans 45071, France*

https://doi.org/10.1021/jacsau.3c00475
JACS Au 2023, 3, 3111−3126

Sung Min Kim − *Department of Mechanical and Process Engineering, ETH Zurich, 8092 Zurich, Switzerland;* orcid.org/0000-0001-6602-1320
Muhammad Awais Naeem − *Department of Mechanical and Process Engineering, ETH Zurich, 8092 Zurich, Switzerland*
Agnieszka Kierzkowska − *Department of Mechanical and Process Engineering, ETH Zurich, 8092 Zurich, Switzerland;* orcid.org/0000-0003-0828-1671
Yi-Hsuan Wu − *Department of Mechanical and Process Engineering, ETH Zurich, 8092 Zurich, Switzerland*
Andac Armutlulu − *Department of Mechanical and Process Engineering, ETH Zurich, 8092 Zurich, Switzerland;* orcid.org/0000-0002-9084-8763

Complete contact information is available at: https://pubs.acs.org/10.1021/jacsau.3c00475

Author Contributions

§M.K. and C.L. contributed equally to this work. CRediT: **Maximilian Krödel** conceptualization, data curation, formal analysis, investigation, methodology, software, visualization, writing-original draft, writing-review & editing; **César Leroy** data curation, formal analysis, investigation, methodology, software, visualization, writing-original draft; **Sungmin Kim** conceptualization, data curation, methodology, writing-review & editing; **Muhammad Awais Naeem** conceptualization, data curation, methodology, writing-review & editing; **Agnieszka M. Kierzkowska** data curation, formal analysis, investigation; **Yi-Hsuan Wu** data curation, formal analysis, investigation, software, writing-review & editing; **Andac Armutlulu** conceptualization, methodology, writing-review & editing; **Alexey Fedorov** conceptualization, funding acquisition, supervision, writing-original draft, writing-review & editing; **Pierre Florian** data curation, formal analysis, methodology, supervision, writing-review & editing; **Christoph R. Müller** conceptualization, funding acquisition, project administration, resources, supervision, writing-review & editing.

Notes

The authors declare no competing financial interest.

■ ACKNOWLEDGMENTS

This research is based on funding by the European Research Council (ERC) under the European Union's Horizon 2020 research and innovation program under grant agreement number 819573. We also acknowledge Foundation Claude & Giuliana for financial support. This publication was created as part of NCCR Catalysis (180544), a National Centre of Competence in Research funded by the Swiss National Science Foundation. The authors acknowledge the help of the ScopeM team at ETH Zürich for SEM, TEM, and EDX analysis. We thank Dr. Felix Donat, Michelle Velvart, and Zixuan Chen for helping with ICP-OES, Raman spectroscopy, and FTIR measurements, respectively. We acknowledge Swiss Laboratories for Materials Science and Technology (EMPA) for access to the XPS facility.

■ REFERENCES

(1) Pachauri, R. K.; Meyer, L. A. *Climate Change 2014: Synthesis Report. Contribution of Working Groups I, II and III to the Fifth Assessment Report of the Intergovernmental Panel on Climate Change.*; 2014.
(2) Krinner, G.; Mxolisi, S.; Bony, S.; Booth, B. B. B.; Brovkin, V.; Browne, O.; Brutel-Vuilmet, C.; Chadwick, R.; Lee, R. W.; Liddicoat, S.; Christopher, L. Long-Term Climate Change: Projections, Commitments and Irreversibility. *Clim. Chang. 2013 Phys. Sci. Basis Work. Gr. I Contrib. to Fifth Assess. Rep. Intergov. Panel Clim. Chang*; Cambridge University Press: Cambridge, United Kingdom, 2013, 9781107057, 10291136
(3) Wei, K.; Guan, H.; Luo, Q.; He, J.; Sun, S. Recent Advances in CO_2 Capture and Reduction. *Nanoscale* **2022**, *14*, 11869−11891.
(4) Boot-Handford, M. E.; Abanades, J. C.; Anthony, E. J.; Blunt, M. J.; Brandani, S.; Mac Dowell, N.; Fernández, J. R.; Ferrari, M. C.; Gross, R.; Hallett, J. P.; Haszeldine, R. S.; Heptonstall, P.; Lyngfelt, A.; Makuch, Z.; Mangano, E.; Porter, R. T. J.; Pourkashanian, M.; Rochelle, G. T.; Shah, N.; Yao, J. G.; Fennell, P. S. Carbon Capture and Storage Update. *Energy Environ. Sci.* **2014**, *7*, 130−189.
(5) Yu, C. H.; Huang, C. H.; Tan, C. S. A Review of CO_2 Capture by Absorption and Adsorption. *Aerosol Air Qual. Res.* **2012**, *12*, 745−769.
(6) Manzolini, G.; Sanchez Fernandez, E.; Rezvani, S.; Macchi, E.; Goetheer, E. L. V.; Vlugt, T. J. H. Economic Assessment of Novel Amine Based CO_2 Capture Technologies Integrated in Power Plants Based on European Benchmarking Task Force Methodology. *Appl. Energy* **2015**, *138*, 546−558.
(7) Bernhardsen, I. M.; Knuutila, H. K. A Review of Potential Amine Solvents for CO_2 Absorption Process: Absorption Capacity, Cyclic Capacity and pKa. *Int. J. Greenh. Gas Control* **2017**, *61*, 27−48.
(8) Dunstan, M. T.; Donat, F.; Bork, A. H.; Grey, C. P.; Müller, C. R. CO_2 Capture at Medium to High Temperature Using Solid Oxide-Based Sorbents: Fundamental Aspects, Mechanistic Insights, and Recent Advances. *Chem. Rev.* **2021**, *121*, 12681−12745.
(9) Krödel, M.; Landuyt, A.; Abdala, P. M.; Müller, C. R. Mechanistic Understanding of CaO-Based Sorbents for High-Temperature CO_2 Capture: Advanced Characterization and Prospects. *ChemSusChem* **2020**, *13*, 6259−6272.
(10) Kierzkowska, A. M.; Pacciani, R.; Müller, C. R. CaO-Based CO_2 Sorbents: From Fundamentals to the Development of New Highly Effective Materials. *ChemSusChem* **2013**, *6*, 1130−1148.
(11) MacKenzie, A.; Granatstein, D. L.; Anthony, E. J.; Abanades, J. C. Economics of CO_2 Capture Using the Calcium Cycle with a Pressurized Fluidized Bed Combustor. *Energy Fuels* **2007**, *21*, 920−926.
(12) Dong, J.; Tang, Y.; Nzihou, A.; Weiss-Hortala, E. Effect of Steam Addition during Carbonation, Calcination or Hydration on Re-Activation of CaO Sorbent for CO_2 capture. *J. CO_2 Util.* **2020**, *39*, No. 101167.
(13) Symonds, R. T.; Lu, D. Y.; Manovic, V.; Anthony, E. J. Pilot-Scale Study of CO_2 Capture by CaO-Based Sorbents in the Presence of Steam and SO_2. *Ind. Eng. Chem. Res.* **2012**, *51*, 7177−7178.
(14) Arias, B.; Grasa, G.; Abanades, J. C.; Manovic, V.; Anthony, E. J. The Effect of Steam on the Fast Carbonation Reaction Rates of CaO. *Ind. Eng. Chem. Res.* **2012**, *51*, 2478−2482.
(15) Sarrión, B.; Perejón, A.; Sánchez-Jiménez, P. E.; Amghar, N.; Chacartegui, R.; Manuel Valverde, J.; Pérez-Maqueda, L. A. Calcination under Low CO_2 Pressure Enhances the Calcium Looping Performance of Limestone for Thermochemical Energy Storage. *Chem. Eng. J.* **2021**, *417*, No. 127922.
(16) Alvarez, D.; Abanades, J. C. Pore-Size and Shape Effects on the Recarbonation Performance of Calcium Oxide Submitted to Repeated Calcination/Recarbonation Cycles. *Energy Fuels* **2005**, *19*, 270−278.
(17) Salaudeen, S. A.; Acharya, B.; Dutta, A. CaO-Based CO_2 Sorbents: A Review on Screening, Enhancement, Cyclic Stability, Regeneration and Kinetics Modelling. *J. CO_2 Util.* **2018**, *23*, 179−199.
(18) Azimi, B.; Tahmasebpoor, M.; Sanchez-Jimenez, P. E.; Perejon, A.; Valverde, J. M. Multicycle CO_2 Capture Activity and Fluidizability of Al-Based Synthesized CaO Sorbents. *Chem. Eng. J.* **2019**, *358*, 679−690.
(19) Kurlov, A.; Broda, M.; Hosseini, D.; Mitchell, S. J.; Pérez-Ramírez, J.; Müller, C. R. Mechanochemically Activated, Calcium Oxide-Based, Magnesium Oxide-Stabilized Carbon Dioxide Sorbents. *ChemSusChem* **2016**, *9*, 2380−2390.
(20) Kim, S. M.; Armutlulu, A.; Kierzkowska, A. M.; Müller, C. R. Inverse Opal-Like, $Ca_3Al_2O_6$-Stabilized, CaO-Based CO_2 Sorbent:

Stabilization of a Highly Porous Structure To Improve Its Cyclic CO_2 Uptake. *ACS Appl. Energy Mater.* **2019**, *2*, 6461−6471.
(21) Kim, S. M.; Liao, W.-C.; Kierzkowska, A. M.; Margossian, T.; Hosseini, D.; Yoon, S.; Broda, M.; Copéret, C. C.; Müller, C. R. In Situ XRD and Dynamic Nuclear Polarization Surface Enhanced NMR Spectroscopy Unravel the Deactivation Mechanism of CaO-Based, $Ca_3Al_2O_6$-Stabilized CO_2 Sorbents. *Chem. Mater.* **2018**, *30*, 1344−1352.
(22) Xu, Y.; Luo, C.; Zheng, Y.; Ding, H.; Wang, Q.; Shen, Q.; Li, X.; Zhang, L. Characteristics and Performance of CaO-Based High Temperature CO_2 Sorbents Derived from a Sol-Gel Process with Different Supports. *RSC Adv.* **2016**, *6*, 79285−79296.
(23) Benitez-Guerrero, M.; Valverde, J. M.; Perejon, A.; Sanchez-Jimenez, P. E.; Perez-Maqueda, L. A. Low-Cost Ca-Based Composites Synthesized by Biotemplate Method for Thermochemical Energy Storage of Concentrated Solar Power. *Appl. Energy* **2018**, *210*, 108−116.
(24) Armutlulu, A.; Naeem, M. A.; Liu, H.-J.; Kim, S. M.; Kierzkowska, A.; Fedorov, A.; Müller, C. R. Multishelled CaO Microspheres Stabilized by Atomic Layer Deposition of Al_2O_3 for Enhanced CO_2 Capture Performance. *Adv. Mater.* **2017**, *29*, No. 1702896.
(25) Broda, M.; Müller, C. R. Sol-Gel-Derived, CaO-Based, ZrO_2-Stabilized CO_2 Sorbents. *Fuel* **2014**, *127*, 94−100.
(26) Sultana, K. S.; Tran, D. T.; Walmsley, J. C.; Rønning, M.; Chen, D. CaO Nanoparticles Coated by ZrO_2 Layers for Enhanced CO_2 Capture Stability. *Ind. Eng. Chem. Res.* **2015**, *54* (36), 8929−8939.
(27) Sanchez-Jimenez, P. E.; Perez-Maqueda, L. A.; Valverde, J. M. Nanosilica Supported CaO: A Regenerable and Mechanically Hard CO_2 Sorbent at Ca-Looping Conditions. *Appl. Energy* **2014**, *118*, 92−99.
(28) Sun, H. Progress in the Development and Application of CaO-Based Adsorbents for CO_2 Capture—a Review. *Mater. Today Sustain.* **2018**, *1-2*, 1−27.
(29) Han, R.; Gao, J.; Wei, S.; Su, Y.; Qin, Y. Development of Highly Effective CaO@Al_2O_3 with Hierarchical Architecture CO_2 Sorbents via a Scalable Limited-Space Chemical Vapor Deposition Technique. *J. Mater. Chem. A* **2018**, *6* (8), 3462−3470.
(30) Wei, S.; Han, R.; Su, Y.; Gao, J.; Zhao, G.; Qin, Y. Pore Structure Modified CaO-Based Sorbents with Different Sized Templates for CO_2 Capture. *Energy Fuels* **2019**, *33*, 5398−5407.
(31) Naeem, M. A.; Armutlulu, A.; Imtiaz, Q.; Donat, F.; Schäublin, R.; Kierzkowska, A.; Müller, C. R. Optimization of the Structural Characteristics of CaO and Its Effective Stabilization Yield High-Capacity CO_2 Sorbents. *Nat. Commun.* **2018**, *9*, No. 2408.
(32) Sun, J.; Liu, W.; Hu, Y.; Li, M.; Yang, X.; Zhang, Y.; Xu, M. Structurally Improved, Core-in-Shell, CaO-Based Sorbent Pellets for CO_2 Capture. *Energy Fuels* **2015**, *29*, 6636−6644.
(33) Krödel, M.; Oing, A.; Negele, J.; Landuyt, A.; Kierzkowska, A.; Bork, A. H.; Donat, F.; Müller, C. R. Yolk-Shell-Type CaO-Based Sorbents for CO_2 Capture: Assessing the Role of Nanostructuring for the Stabilization of the Cyclic CO_2 Uptake. *Nanoscale* **2022**, *14*, 16816−16828.
(34) Ping, H.; Wu, S. CO_2 Sorption Durability of Zr-Modified Nano-CaO Sorbents with Cage-like Hollow Sphere Structure. *ACS Sustain. Chem. Eng.* **2016**, *4*, 2047−2055.
(35) Sun, H.; Wang, Y.; Xu, S.; Osman, A. I.; Stenning, G.; Han, J.; Sun, S.; Rooney, D.; Williams, P. T.; Wang, F.; Wu, C. Understanding the Interaction between Active Sites and Sorbents during the Integrated Carbon Capture and Utilization Process. *Fuel* **2021**, *286*, No. 119308.
(36) Kim, S. M.; Armutlulu, A.; Kierzkowska, A. M.; Hosseini, D.; Donat, F.; Müller, C. Development of an Effective Bi-Functional Ni−CaO Catalyst-Sorbent for the Sorption-Enhanced Water Gas Shift Reaction through Structural Optimization and the Controlled Deposition of a Stabilizer by Atomic Layer Deposition. *Sustain. Energy Fuels* **2020**, *4*, 713−729.
(37) Kurlov, A.; Armutlulu, A.; Donat, F.; Studart, A. R.; Müller, C. R. CaO-Based CO_2 Sorbents with a Hierarchical Porous Structure Made via Microfluidic Droplet Templating. *Ind. Eng. Chem. Res.* **2020**, *59*, 7182−7188.
(38) Kaushik, M.; Leroy, C.; Chen, Z.; Gajan, D.; Willinger, E.; Müller, C. R.; Fayon, F.; Massiot, D.; Fedorov, A.; Copéret, C.; Lesage, A.; Florian, P. Atomic-Scale Structure and Its Impact on Chemical Properties of Aluminum Oxide Layers Prepared by Atomic Layer Deposition on Silica. *Chem. Mater.* **2021**, *33*, 3335−3348.
(39) Wagner, C. D.; Naumkin, A. V.; Kraut-Vass, A.; Allison, J.W.; Powell, J. C.. *NIST Standard Reference Database 20*.
(40) Reddy, N.; Bera, P.; Reddy, V. R.; Sridhara, N.; Dey, A.; Anandan, C.; Sharma, A. K. XPS Study of Sputtered Alumina Thin Films. *Ceram. Int.* **2014**, *40*, 11099−11107.
(41) Liu, Y.; Zeng, F.; Sun, B.; Jia, P.; Graham, I. T. Structural Characterizations of Aluminosilicates in Two Types of Fly Ash Samples from Shanxi Province North China. *Minerals* **2019**, *9*, 358.
(42) Demri, B.; Muster, D. XPS Study of Some Calcium Compounds. *J. Mater. Process. Technol.* **1995**, *55*, 311−314.
(43) Ni, M.; Ratner, B. D. Differentiating Calcium Carbonate Polymorphs by Surface Analysis Techniques - An XPS and TOF-SIMS Study. *Surf. Interface Anal.* **2008**, *40*, 1356−1361.
(44) Hallstedl, B. Assessment of the CaO-Al_2O_3 System. *J. Am. Ceram. Soc.* **1990**, *73*, 15−23.
(45) Li, L.; King, D. L.; Nie, Z.; Howard, C. Magnesia-Stabilized Calcium Oxide Absorbents with Improved Durability for High Temperature CO_2 Capture. *Ind. Eng. Chem. Res.* **2009**, *48*, 10604−10613.
(46) Li, Z.-S.; Fang, F.; Tang, X.-Y.; Cai, N.-S. Effect of Temperature on the Carbonation Reaction of CaO with CO_2. *Energy Fuels* **2012**, *26*, 2473−2482.
(47) Lu, S.; Lin, Q.; Wu, S. Synergy of Pore Size and Specific Surface Area on the CO_2 Sorption Performance of Nano CaO-Based Sorbents. *J. Nanosci. Nanotechnol.* **2019**, *19*, 3205−3209.
(48) Wang, C.; Zhou, X.; Jia, L.; Tan, Y. Sintering of Limestone in Calcination/Carbonation Cycles. *Ind. Eng. Chem. Res.* **2014**, *53*, 16235−16244.
(49) Hong, J.; Heo, S. J.; Singh, P. Water Mediated Growth of Oriented Single Crystalline $SrCO_3$ Nanorod Arrays on Strontium Compounds. *Sci. Rep.* **2021**, *11*, No. 3368.
(50) Beruto, D.; Searcy, A. W. Calcium Oxides of High Reactivity. *Nature* **1976**, *263*, 221−222.
(51) Sun, Z.; Luo, S.; Qi, P.; Fan, L.-S. Ionic Diffusion through Calcite ($CaCO_3$) Layer during the Reaction of CaO and CO_2. *Chem. Eng. Sci.* **2012**, *81*, 164−168.
(52) Hjorth, J.; Skibsted, J.; Jakobsen, H. J. ^{29}Si MAS NMR Studies of Portland Cement Components and Effects of Microsilica on the Hydration Reaction. *Cem. Concr. Res.* **1988**, *18*, 789−798.
(53) Lippmaa, E.; Magi, M.; Samoson, A.; Engelhard, G.; Grimmer, A. R. Structural Studies of Silicates by Solid-State High-Resolution ^{29}Si NMR. *J. Am. Chem. Soc.* **1980**, *102*, 4889−4893.
(54) Mägi, M.; Lippmaa, E.; Samoson, A.; Engelhardt, G.; Grimmer, A. R. Solid-State High-Resolution Silicon-29 Chemical Shifts in Silicates. *J. Phys. Chem.* **1984**, *88*, 1518−1522.
(55) Wang, Y.; Zhao, Q.; Zhou, S.; Wang, S. Effect of C/S Ratio on Microstructure of Calcium Silicate Hydrates Synthesised by Solution Reaction Method. *IOP Conf. Ser. Mater. Sci. Eng.* **2019**, *472*, No. 012003.
(56) Méducin, F.; Bresson, B.; Lequeux, N.; de Noirfontaine, M. N.; Zanni, H. Calcium Silicate Hydrates Investigated by Solid-State High Resolution ^{1}H and ^{29}Si Nuclear Magnetic Resonance. *Cem. Concr. Res.* **2007**, *37*, 631−638.
(57) Yan, F.; Jiang, J.; Li, K.; Tian, S.; Liu, Z.; Shi, J.; Chen, X.; Fei, J.; Lu, Y. Cyclic Performance of Waste-Derived SiO_2 Stabilized, CaO-Based Sorbents for Fast CO_2 Capture. *ACS Sustain. Chem. Eng.* **2016**, *4*, 7004−7012.
(58) Huang, C.; Xu, M.; Huai, X.; Liu, Z. Template-Free Synthesis of Hollow CaO/Ca_2SiO_4 Nanoparticle as a Cyclically Stable High-Capacity CO_2 Sorbent. *ACS Sustain. Chem. Eng.* **2021**, *9*, 2171−2179.

https://doi.org/10.1021/jacsau.3c00475
JACS Au 2023, 3, 3111−3126

(59) Hauch, A.; Bildsøe, H.; Jakobsen, H. J.; Skibsted, J. ^{29}Si Chemical Shift Anisotropies from High-Field ^{29}Si MAS NMR Spectroscopy. *J. Magn. Reson.* **2003**, *165*, 282−292.
(60) Smith, M. E. Application Of ^{27}Al NMR Techniques to Structure Determination in Solids. *Appl. Magn. Reson.* **1993**, *4*, 1−64.
(61) Edén, M. Update on ^{27}Al NMR Studies of Aluminosilicate Glasses. *Annu. Rep. NMR Spectrosc.* **2020**, *101*, 285−410.
(62) Edén, M. *^{27}Al NMR Studies of Aluminosilicate Glasses*, 1st ed.; 2015; *86*.
(63) Walkley, B.; Provis, J. L. Solid-State Nuclear Magnetic Resonance Spectroscopy of Cements. *Mater. Today Adv.* **2019**, *1*, No. 100007.
(64) Haouas, M.; Taulelle, F.; Martineau, C. Recent Advances in Application of ^{27}Al NMR Spectroscopy to Materials Science. *Prog. Nucl. Magn. Reson. Spectrosc.* **2016**, *94*−*95*, 11−36.
(65) Skibsted, J.; Henderson, E.; Jakobsen, H. J. Characterization of Calcium Aluminate Phases in Cements by ^{27}Al MAS NMR Spectroscopy. *Inorg. Chem.* **1993**, *32*, 1013−1027.
(66) Alzeer, M. I. M.; Nguyen, H.; Fabritius, T.; Sreenivasan, H.; Telkki, V. V.; Kantola, A. M.; Cheeseman, C.; Illikainen, M.; Kinnunen, P. On the Hydration of Synthetic Aluminosilicate Glass as a Sole Cement Precursor. *Cem. Concr. Res.* **2022**, *159*, No. 106859.
(67) Jerebtsov, D. A.; Mikhailov, G. G. Phase Diagram of CaO-Al_2O_3 System. *Ceram. Int.* **2001**, *27*, 25−28.
(68) Naeem, M. A.; Armutlulu, A.; Kierzkowska, A.; Müller, C. R. Development of High-Performance CaO-Based CO_2 Sorbents Stabilized with Al_2O_3 or MgO. *Energy Procedia* **2017**, *114*, 158−166.
(69) Neuville, D. R.; Cormier, L.; Massiot, D. Al Coordination and Speciation in Calcium Aluminosilicate Glasses: Effects of Composition Determined by ^{27}Al MQ-MAS NMR and Raman Spectroscopy. *Chem. Geol.* **2006**, *229*, 173−185.
(70) Scardi, P.; Sartori, N.; Giachello, A.; Demaestri, P. P.; Branda, F. Influence of Calcium Oxide and Sodium Oxide on the Microstructure of Cordierite Catalyst Supports. *Ceram. Int.* **1993**, *19*, 105−111.
(71) Freitas, A. A.; Santos, R. L.; Colaço, R.; Bayão Horta, R.; Canongia Lopes, J. N. From Lime to Silica and Alumina: Systematic Modeling of Cement Clinkers Using a General Force-Field. *Phys. Chem. Chem. Phys.* **2015**, *17*, 18477−18494.
(72) Tandia, A.; Timofeev, N. T.; Mauro, J. C.; Vargheese, K. D. Defect-Mediated Self-Diffusion in Calcium Aluminosilicate Glasses: A Molecular Modeling Study. *J. Non-Cryst. Solids* **2011**, *357*, 1780−1786.
(73) Zheng, K.; Yang, F.; Wang, X.; Zhang, Z. Investigation of Self-Diffusion and Structure in Calcium Aluminosilicate Slags by Molecular Dynamics Simulation. *Mater. Sci. Appl.* **2014**, *05*, 73−80.
(74) Skibsted, J.; Jakobsen, H. J.; Hall, C. Direct Observation of Aluminium Guest Ions in the Silicate Phases of Cement Minerals by ^{27}Al MAS NMR Spectroscopy. *J. Chem. Soc. Faraday Trans.* **1994**, *90*, 2095−2098.
(75) Nadjafi, M.; Kierzkowska, A. M.; Armutlulu, A.; Verel, R.; Fedorov, A.; Abdala, P. M.; Müller, C. R. Correlating the Structural Evolution of ZnO/Al_2O_3 to Spinel Zinc Aluminate with Its Catalytic Performance in Propane Dehydrogenation. *J. Phys. Chem. C* **2021**, *125*, 14065−14074.
(76) Dingemans, G.; Van Helvoirt, C.; Van de Sanden, M. C. M.; Kessels, W. M. Plasma-Assisted Atomic Layer Deposition of Low Temperature SiO_2. *ECS Trans.* **2011**, *35*, 191−204.
(77) Rodriguez-Carvajal, J. FULLPROF: A Program for Rietveld Refinement and Pattern Matching Analysis. *Abstracts of the Satellite Meeting on Powder Diffraction of the XV Congress of the IUCr*, **1990**, *127*.
(78) Donat, F.; Müller, C. R. A Critical Assessment of the Testing Conditions of CaO-Based CO_2 Sorbents. *Chem. Eng. J.* **2018**, *336*, 544−549.
(79) Lippmaa, E.; Samoson, A.; Mägi, M. High-Resolution ^{27}Al NMR Aluminosilicates. *J. Am. Chem. Soc.* **1986**, *108*, 1730−1735.
(80) Massiot, D.; Fayon, F.; Capron, M.; King, I.; Le Calvé, S.; Alonso, B.; Durand, J. O.; Bujoli, B.; Gan, Z.; Hoatson, G. Modelling One- and Two-Dimensional Solid-State NMR Spectra. *Magn. Reson. Chem.* **2002**, *40*, 70−76.
(81) Yon, M.; Fayon, F.; Massiot, D.; Sarou-Kanian, V. Iterative Baseline Correction Algorithm for Dead Time Truncated One-Dimensional Solid-State MAS NMR Spectra. *Solid State Nucl. Magn. Reson.* **2020**, *110*, No. 101699.
(82) Kentgens, A. P. M.; Verhagen, R. Advantages of Double Frequency Sweeps in Static, MAS and MQMAS NMR of Spin I = 3/2 Nuclei. *Chem. Phys. Lett.* **1999**, *300*, 435−443.
(83) Iuga, D.; Schäfer, H.; Verhagen, R.; Kentgens, A. P. M. Population and Coherence Transfer Induced by Double Frequency Sweeps in Half-Integer Quadrupolar Spin Systems. *J. Magn. Reson.* **2000**, *147*, 192−209.
(84) Shirley, D. A. High-Resolution X-Ray Photoemission Spectrum of the Valence Bands of Gold. *Phys. Rev. B* **1972**, *5*, 4709.
(85) Scofield, J. H. Hartree-Slater Subshell Photoionization Cross-Sections at 1254 and 1487 eV. *J. Electron. Spectrosc. Relat. Phenom.* **1976**, *8*, 129−137.

https://doi.org/10.1021/jacsau.3c00475
JACS Au 2023, 3, 3111−3126